Nanoscale effect on the formation of the amorphous Ni silicide by rapid thermal annealing from crystalline and pre-amorphized silicon

C. Delwail, K. Dabertrand, S. Joblot, F. Mazen, D. Mangelinck

Nanoscale effect on the formation of the amorphous Ni silicide by rapid thermal annealing from crystalline and pre-amorphized silicon

C. Delwail [1,2,3], K. Dabertrand [2], S. Joblot [2], F. Mazen[3], D. Mangelinck[1]

[1] *Aix-Marseille Université, CNRS, Institut Matériaux Microélectronique Nanosciences de Provence, Faculté de Saint Jérôme, 13397 Marseille Cedex 20, France*

[2] *STMicroelectronics, 850, rue Jean Monnet, 38926, Crolles cedex, France*

[3] *Université Grenoble Alpes, CEA-LETI, F-38000 Grenoble, France*

Abstract

The Ni monosilicide alloyed with Pt is widely used as contact material in advanced microelectronics devices and a good knowledge of silicide formation kinetics is required for the process control. In this work, the nature, and the growth kinetics of the first silicide obtained during the solid-state reaction between the $Ni_{0.9}Pt_{0.1}$ and the Si are studied for different pre amorphization implant (PAI) conditions as well as for a reference sample without PAI. Reactions between a 10 nm thick $Ni_{0.9}Pt_{0.1}$ film and Si (100) substrate are analyzed after several rapid thermal anneals (RTA). The nature of the first silicide is determined by Fourier Transform of TEM images and by chemical TEM-EDX analyses. The silicide growth behavior is determined by measuring the silicide thickness by X ray reflectivity (XRR) after the partial reaction induced by RTAs at different temperatures and times. To determine the growth law, the linear parabolic model is first considered but a nonlinear reactive diffusion model must be developed to accurately reproduce the experimental results. From this model, the effective diffusion coefficient as well as its activation energy were determined for the three samples with PAI and the reference sample without PAI. The influence of the driving force on the nonlinear diffusion for thin films is proved, and the impact of the amorphous substrate on the kinetics parameters is quantified and compared to the literature.

1. Introduction

Silicides are used in microelectronics devices as contacts and are obtained by solid state reaction between a thin metal film and a Si substrate. For technology nodes below 65 nm, and even for the most advanced planar geometry, the Ni silicide is the preferred material because of its low resistivity as well as the low thermal budget and low Si consumption required for the NiSi formation [1]. Nevertheless, the NiSi has two major drawbacks. Firstly, the resistive $NiSi_2$ phase nucleates at the expense of NiSi around 750°C. Secondly, NiSi thin films with thickness below 30 nm are not stable for temperatures around 600°C due to agglomeration issues. Moreover, agglomeration becomes more stringent when the silicide thickness is decreased to follow the devices downscaling required in microelectronics. These issues are partly solved with the addition of Pt to the Ni. Thereby, the Pt alloyed to the Ni allows to extend the thermal stability up to 900°C [2], without drastically changing the Ni-silicides advantages. In addition, Detavernier et al. [3] report that the addition of Pt to the Ni reduces the importance of the axiotaxy

between the NiSi and the Si and this modification of the silicide texture is assumed to reduce the agglomeration. Consequently, for 28 nm FDSOI technologies node devices, the $Ni_{0.9}Pt_{0.1}$ mono silicide is the actual contact material [4,5]. The $Ni_{0.9}Pt_{0.1}$ silicide phase sequence, kinetics parameters and properties were extensively studied [6–14]. For thin thicknesses (~10 nm), the reaction between $Ni_{0.9}Pt_{0.1}$ and the Si results in a sequential growth: the θ-Ni_2Si phase grows first, and, once the $Ni_{0.9}Pt_{0.1}$ layer is totally consumed, the NiSi phase grows at the expense of the θ-Ni_2Si layer. Even if the thermal stability is improved with the addition of Pt, the agglomeration phenomenon is still an issue, particularly for thin silicide layers around 10 nm.

The amorphization of Si before silicidation using Pre-Amorphization ion Implantation (PAI) has been intensively employed to further improve the silicide properties. Van Stiphout et al. [15,16] have reported that the PAI modifies the kinetics and the phase sequence of the Ni silicide depending on the implantation parameters. Indeed, for Ar PAI, the NiSi nucleation temperature is reduced while it is increased for N PAI with increasing fluence. In addition, an improvement in thermal stability has been related to a NiSi axiotaxy loss due to a high incorporation of N into the silicide layer. Furthermore, it was observed that, for the highest fluences of nitrogen, the phase sequence changes since the θ-Ni_2Si phase is no longer formed but an amorphous phase, a-$Ni_{1-x}Si_x$, grows instead. A similar change in phase sequence has also been reported by Guillemin et al. [17] for a dual Ge/C PAI. Guillemin et al. [17] and Lachal et al. [18] have also shown that carbon has significant effects on the growth kinetics of the first silicide during in-situ annealing. Moreover, Guillemin et al. [17] , Lachal et al. [18] , and Ozcan et al. [19] have put forward the influence of the amorphous silicon (a-Si) thickness on the silicide properties and kinetics. In particular, Lachal *et al.* [18] have shown that the silicide roughness, the thermal stability and the resistivity can be improved depending of the PAI process used. Moreover, a clear dependence with the a-Si thickness formed during the implantation was evidenced [18].

These improvements and kinetics changes indicate that the damaged or amorphous Si has an influence on the silicidation process. However, the kinetics and mechanisms related to these changes have not been deeply investigated. In particular, the kinetics of formation of the first silicide is of great importance when a partial silicidation is performed during the silicide process since it allows to precisely control the final thickness of the contact. Indeed, in the self-aligned silicide process (salicide) with partial silicidation, a given thickness of first silicide is formed during the first rapid thermal anneal (RTA) by selecting the thermal budget and, after selective etch of the unreacted metal, is converted in NiSi with the desired thickness during the second rapid thermal anneal. In this work, the nature of the first phase to grow is studied for different PAI conditions. The growth kinetics of the first silicide is investigated in detail and a new model considering nonlinear diffusion is proposed for the growth law.

2. Experimental procedure

300 mm diameter p-type Si (100) blanket wafers with a resistivity of 20-40 $\Omega.\mathrm{cm}$ were used. The different steps involved in the sample preparation and analysis are summarized in Fig. 1. To determine the effect of the PAI on the growth kinetics of the first silicide, three different kinds of PAI were performed

and compared to a reference sample (without PAI). Prior to the PAI step, the samples were deoxidized using a HF/HCL solution. Then, Ge and C implantations were performed in a high current ion implanter, with the following conditions: current intensity of 2 mA for the Ge implantation and 1.4 mA for the C implantation with a static ribbon shape of approximatively 100 cm², 35 cm width and few centimeters height. Fig. 1 describes the three different implantation conditions carried out to study the growth kinetics of the first silicide. The amorphous silicon (a-Si) thicknesses were estimated by TCAD simulation with the KMC model using the Synopsys Sentaurus process simulator [20]. The three PAI conditions were chosen to induce an amorphous thickness (a-Si) of 25 nm. The as implanted samples were then characterized by TEM analyses to control the coherence between the targeted and measured thicknesses. TEM analyses show that a-Si is ~ 26 nm thick for all the samples (not shown here). Therefore, for all the samples, the silicide formation takes place with the a-Si (i.e., the a-Si is not completely consumed during annealing).

The first Ge PAI ($1x10^{14}$ at/cm^3, 20 keV) induces a layer partially amorphized with crystalline islands on the surface while the second Ge PAI ($9x10^{14}$ at/cm^3, 13 keV) induces a homogeneous amorphous layer. Finally, the third PAI condition chosen is a germanium ($9x10^{14}$ at/cm^3, 13 keV) then carbon ($4x10^{15}$ at/cm^3, 3 keV) co-implantation. This Ge+C PAI was chosen based on the studies of Lachal et al. [18] and Guillemin et al. [17]. The goal of this Ge+C PAI is to highlight and quantify the effect of C on the kinetics of formation of the first silicide during rapid annealing (RTA). The PAI parameters and characteristics of the induced amorphous layer are detailed in appendix A. In addition to the PAI samples, a sample without PAI was also used as reference.

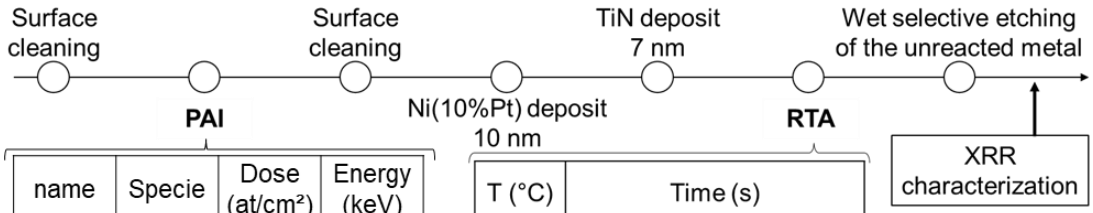

name	Specie	Dose (at/cm²)	Energy (keV)
Q1	Ge	$1x10^{14}$	20
Q2	Ge	$9x10^{14}$	13
Q3	Ge	$9x10^{14}$	13
	C	$4x10^{15}$	3
Q4	Reference (without PAI)		

T (°C)	Time (s)
230	10, 30, 55, 80, 100
220	10, 50, 90, 140, 165
210	10, 100, 190, 290, 360
200	10, 320, 900, 1500, 2000

Fig. 1. Step sequence used to develop and characterize the samples including the details of the PAI and annealing conditions. Three PAI conditions were chosen to compare the growth kinetics of the first silicide. For each of these PAI conditions, all the annealings were applied individually. Thus, each implantation condition involves 20 different samples that were characterized by X-ray reflectivity (XRR) after selective removal of unreacted metal.

Prior to the film deposition, the Si wafers were cleaned using a HF/HCL solution followed by an in situ chemical etch and anneal process (Siconi™ Process [21]). A 10 nm $Ni_{0.9}Pt_{0.1}$ layer and a capping layer of 7 nm thick TiN were then both deposited by magnetron sputtering (Endura equipment of Applied Materials) without vacuum breaking between the two depositions. The NiPt deposition was performed from a Ni(Pt10%) target and the TiN from a titanium target and nitrogen-controlled environment.

The TiN/$Ni_{0.9}Pt_{0.1}$ layers deposited on the different samples were then submitted to rapid thermal anneals (RTA) for five different times at temperatures ranging from 200 to 230°C (Fig. 1). These times were chosen to keep the reaction partial (i.e., the NiPt layer not fully consumed) and then to be able to measure thickness variations depending on the RTA process. To ensure that all the reactions are partial, each sample was analyzed by X-ray reflectivity (XRR) after each RTA to verify the presence of a layer of NiPt between the TiN and the silicide. However, the unreacted NiPt and TiN capping were finally removed by wet selective etching for the precise determination of the silicide thickness since the XRR curves for a single layer are much less complex and easier to simulate. Then the JVXRSS software was used to simulate the XRR curves with a model considering the gradient of Pt distribution found by Panciera [22]. The silicide thickness was precisely determined (± 0.1 nm) for each sample (the model used, and an example of the fitted data are given in appendix B). The nature of the first silicide was determined by TEM analysis. A Fourier transform applied on the TEM images was used to determine the crystallinity of the silicide. A chemical analysis carried out by EDX (Electron Dispersive X-Ray) spectroscopy was also performed to complete the analyses of the first silicide.

3. Results

Fig. 2.a shows a TEM micrograph of the reference sample after a RTA at 230°C for 20 s. The silicide forms a homogeneous thin film about 8 nm thick in agreement with XRR measurements (not shown here). The contrast in the silicide indicates an amorphous nature of the silicide film. This is confirmed by the fast Fourier transform shown in Fig. 2.b and by diffraction patterns (not shown here) that show concentric rings characteristic of an amorphous phase. Similar results were obtained for samples with PAI. Fig. 2.c shows the result of the chemical analysis carried out by EDX spectroscopy. As the quantification is biased by the chemical environment, in particular by the oxygen at the surfaces of the TEM slides, the atomic percentages indicated on the graph should not be considered as absolute value but as relative ones. The shape as well as the relative distributions of Ni, Si and Pt were similar for all the samples (with or without PAI) and showed the same characteristics. First, the Pt is not uniformly distributed, it is localized closer to the surface in the first half of the silicide. This observation agrees with the analyses carried out using APT by Panciera et al. [22]. Furthermore, the Si concentration shows that the silicide becomes richer in Si when going from the surface towards the interface: the silicide composition is therefore not constant, in accordance with APT measurements [11,22]. Thus, the silicide presents a non-stoichiometric composition, which would be consistent with the presence of an amorphous phase but could also correspond to the non-stoichiometric crystalline phase, θ-Ni_2Si [23].

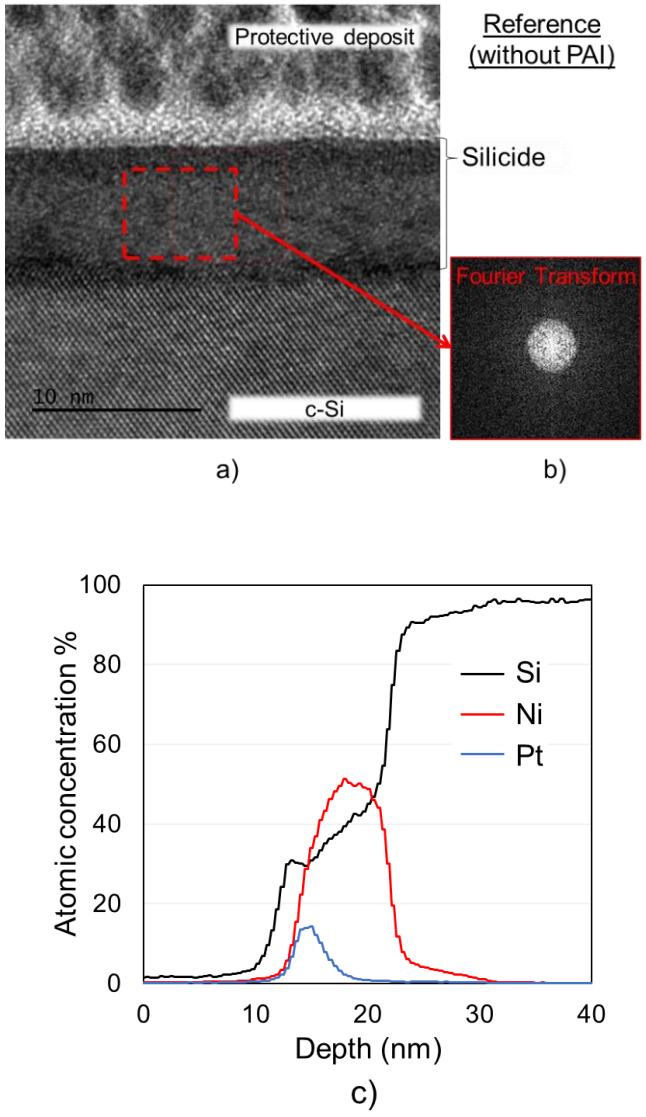

Fig. 2. a) TEM micrography for the reference sample without PAI after the RTA b) Fourier transform of the region corresponding to the silicide c) Distribution of the chemical elements of the silicide measured by X-ray spectroscopy (EDX) carried out from the TEM slides of the reference sample.

To conclude, our results show that, in our experimental conditions, the silicide which forms during RTA corresponds to a non-stochiometric amorphous phase. This amorphous silicide will be denoted as a-$Ni_{1-x}Si_x$ in the following even if it contains some Pt. Its formation instead of the θ-Ni_2Si phase will be discussed later.

The growth kinetics of the first silicide during RTA type annealing was determined by XRR measurements of the silicide thickness. These measurements were performed after the different annealing duration and temperatures listed in Fig. 1 for the three samples with different PAI conditions as well as for the reference without PAI.

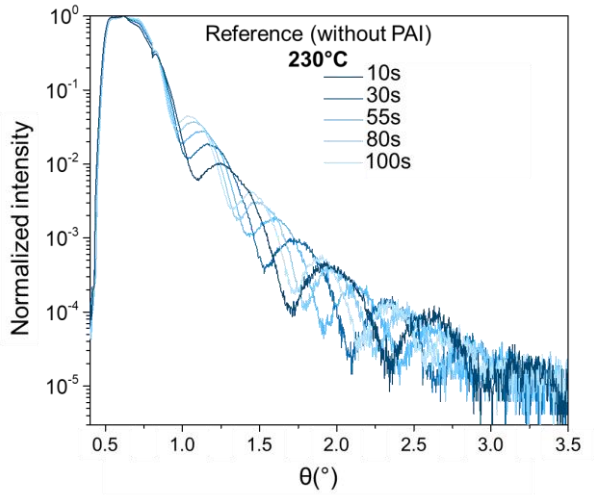

Fig. 3. X-ray reflectivity curves (XRR) for the reference samples having undergone a thermal budget of 230°C for 10, 30, 55, 80 and 100 seconds.

Fig. 3 shows the XRR curves for the reference samples having undergone an RTA at 230°C for 10, 30, 55, 80 and 100 s respectively. The period of the oscillations gradually decreases with the annealing duration, illustrating the evolution of the thickness according to the applied thermal budget. For each sample, the thickness of the first silicide was determined by simulation of the XRR curves.

Fig. 4 shows the evolution of the silicide thickness as a function of the temperature and the annealing duration for the samples with the different PAI conditions as well as for the reference sample without PAI. The silicide thickness logically increases with annealing duration. For all the samples with or without PAI, the growing rate (slope of the curve) is slowing down with increasing time as expected for a parabolic or linear-parabolic growth rate. This slowing-down is more pronounced at lower temperatures than at higher temperatures. The silicide thickness of the samples with low and high Ge PAI fluences is greater than that of the reference samples without PAI and with the Ge+C PAI. This difference widens with the annealing duration. Moreover, for Ge PAI processes, the silicide thickness is slightly greater for the sample with the lowest concentration of implanted ions during the PAI. This suggests that the kinetics formation could depend on the Ge concentration, the defect concentration and/or on the amorphous layer properties (partial amorphization for the lowest fluence). These observations are consistent with the variations in the rate of formation of the first silicide observed as a function of the amorphous thickness and the concentration of Ge ions implanted in our previous work [24]. Finally, the Ge+C PAI induces lower thicknesses than those obtained with Ge PAI and the thicknesses are almost equal to those of the reference sample. Therefore, the Ge+C PAI sample appears to slows down the rate of formation of the silicide as reported previously [17,18].

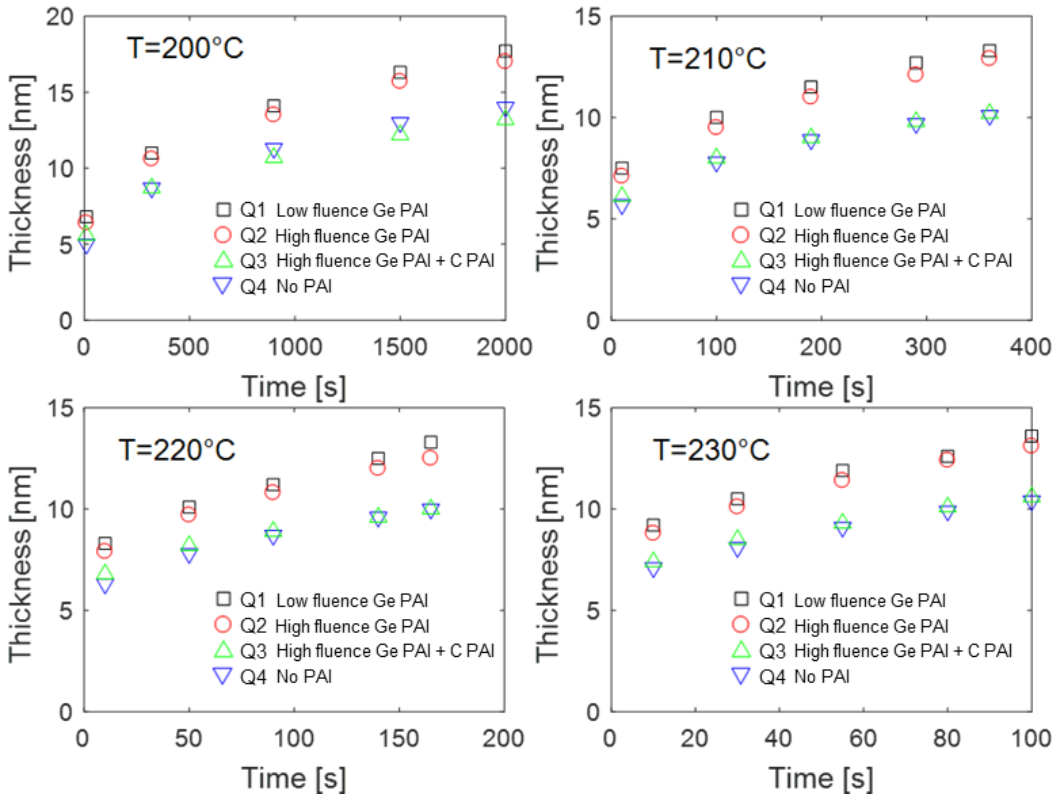

Fig. 4. Thickness obtained by XRR for different times at temperature of a) 200°C, b) 210°C, c) 220°C, d) 230°C for the reference and PAI samples.

4. Discussion

Our results for the reference sample (Fig. 2) and other TEM analysis for the PAI samples (not shown here) show that the silicide is mainly amorphous after RTA and selective removal. In situ XRD measurements (not shown here) are also in agreement with the formation of an amorphous silicide as the first growing phase since no new diffraction peak is observed while there is consumption of the metal (disappearance of the diffraction peak of the metal). Concerning the composition of the first silicide, the analysis by TEM-EDX (Fig. 2.c) indicates the presence of a composition gradient ranging from approximately 30 to 48% of Si (note that these concentrations are determined by including the oxygen coming from the contamination of the TEM lamella). This Si gradient is in agreement with an amorphous phase and/or the θ-Ni_2Si phase since these two phases are non-stoichiometric phases [23] whereas the other phases usually observed (δ-Ni2Si and NiSi) are stoichiometric. Moreover, the Pt atoms, present mainly towards the surface of the sample, are strongly incorporated since there is up to 20% of Pt in the silicide. This concentration is much higher than the initial 10 at. % in the Ni(Pt) alloy (note that due to the presence of Si in the silicide, this concentration corresponds to a Pt/(Ni+Pt) ratio of about 30%). This strong incorporation and the strong Pt concentration gradient are two characteristics of the θ-Ni_2Si phase [10,25] and could also be explained in an amorphous phase which is characterized by significant

disorder and therefore a possibility of "accommodating" different atoms. On the contrary, Pt is poorly soluble in the stoichiometric δ-Ni_2Si phase [26].

4.1. Amorphous Ni silicide

It appears thus that the first phase to grow in our case is an amorphous silicide in contrast to the θ-Ni_2Si phase usually found as first silicide during the reaction of Ni(10% Pt) film with (100)Si [7,11–13,25,27]. Note that by first silicide we refer to the first phase which grows during the annealing. It should also be specified that the nature of the first Ni silicide which grows in a thin film is difficult to determine by: (i) the number of possible phases (δ-Ni_2Si, θ-Ni_2Si, $Ni_{31}Si_{12}$, Ni_3Si_2, amorphous…) (ii) the relative complexity of the crystalline phases which gives many diffraction peaks close to each other (iii) their close composition (iv) their texture which is generally strong including the possibility of epitaxy (v) the variability of the nature of the phases according to the thickness of the metal deposited as well as the presence of alloying elements and/or impurities.

In the studies in which θ-Ni_2Si was detected[7,11,13,25,27], the Pt percentages were between 10 and 13% and the NiPt thicknesses between 3 and 25 nm. According to these studies, for our samples with 10 nm of Ni(10%Pt), the first silicide should be the θ-Ni_2Si phase. Thus, the percentage of Pt and the thickness of NiPt do not explain why the nature of the first silicide differs in our samples from what was reported previously.

Indeed, the nature of the first silicide that grows results from thermodynamic and kinetics competition between the different phases likely to form. To win this competition, the silicide must first nucleate and then grow faster than the others. The nucleation barrier of a phase depends on the nucleation driving force and the energy needed to create the new interfaces, but a necessary condition is also that the local composition corresponds to the nucleating phase. This usually requires the transport and reorganization of atoms. Therefore, the mobility and the ability of atoms to rearrange during silicidation is an important parameter. After nucleation, the growth is characterized by two stages [28]: (i) lateral growth which allows the formation of a continuous layer from the seeds formed at the interface and (ii) normal growth during which the thickness of the phase increases. The kinetics of these mechanisms depends on the driving force and on the atomic transport [28]. This transport is mainly along interfaces for lateral growth and mainly through the forming phase for normal growth (in both cases transport through the forming phase plays a role). In polycrystalline thin films, grain boundary diffusion plays a major role.

The case of amorphous silicides is more special because a condition for forming an amorphous phase by reaction in the solid state is that one of the species must be highly mobile over a large distance relative to the other species which has a very low mobility [29]. This asymmetry leads to a diffusion flow of the dominant species which maintains a rapid growth at the growth front. Thus, the growth front leaves behind an amorphous silicide since the low mobility of the less mobile species prevents their

reorganization necessary to allow the formation of a crystalline phase [29]. The formation of a crystalline silicide layer is therefore inhibited.

After recalling these basic notions on the formation of the first phase, we will consider the influence of silicidation processes considering thermodynamics and kinetics to identify the different elements likely to influence the nature of the first silicide and promote the growth of an amorphous silicide. Indeed, several aspects related to the processes used during the silicidation could influence the nature of the first silicide such as the thermal budget, the thickness of Ni consumed [15,16], the TiN encapsulation, the surface preparation before the metal deposition [12] [30] or the metal deposition itself.

The surface preparation before the metal deposition and the metal deposition are steps of the silicide elaboration that can exert an influence on the nature of the first silicide. For example, Imbert et al. [30] have shown that the surface preparation before Ni(5%Pt) deposition can alter the phase sequence. Indeed, the first silicide was found to depend on the surface preparation : in situ argon sputtering etch, in situ remote plasma and standard wet HF clean. For these three different surface preparations, the first induces the formation of the δ-Ni_2Si phase, the second Ni_3Si_2 and no XRD peak was detected for the third ones indicating the formation of either an epitaxial phase or an amorphous phase [30]. This last observation is like the Ni(10%Pt) case and suggests that surface preparation could induce the formation of an amorphous silicide.

Moreover, the physical and chemical surface preparation can have the effect of modifying the surface composition of the substrate. Some atoms, originating from the plasma or from the native oxide, can be implanted on the surface of the substrate and modify the composition of the mixing layer. This effect was demonstrated by El Kousseifi et al. [12] who showed that the incorporation of Pt in the mixing layer influences the formation of the first silicide. By changing the composition near the interface using different deposits, this study has shown that the first growing phase depends on the composition of the mixing layer. When the mixed layer contains Pt, the θ-Ni_2Si phase is formed, otherwise the δ-Ni_2Si phase grows. This behavior was explained by considering nucleation and the difference in solubility of Pt in θ-Ni_2Si and δ-Ni_2Si that changes the driving forces of nucleation. This example illustrates that the composition of the mixing layer, which can depend on the surface preparation, can determine the nature of the first silicide. Therefore, the type and the characteristics of the deposition can modify the composition of the mixture layer and influence the nature of the first silicide.

In addition to the thermodynamic aspect on the driving forces, the presence of impurities or alloying elements can influence the kinetics by creating a diffusion barrier at the interface and/or by modifying the diffusion in the growing phase. Indeed, as explained above, the formation of the amorphous phase by solid state reaction generally results from a large diffusion asymmetry between the two species because the rapid growth due to the diffusion of the fast species does not allow the reorganization necessary for the formation of a crystalline phase, this reorganization being linked to the mobility of the less mobile species. Factors that increase the diffusion asymmetry can therefore also induce the

formation of the amorphous phase. For example, the Xe implantation at 200°C in a stack was shown to lead to the formation of an amorphous phase during a solid-state reaction by accelerating the migration rate over a long distance of the more mobile species [31]. In the Ni silicides, it is generally the Ni atoms that diffuses mainly, and this also seems to be the case during the reaction between NiPt and Si [25]. Thus, a mechanism which increases the diffusion of Ni atoms and/or slows down that of Si atoms could favor the formation of the amorphous silicide.

Van Stiphout et al. [15,16] have recently shown that nitrogen implantation at the interface leads to the formation of an amorphous phase by reaction between Ni films with thickness equal to 13 to 35 nm and Si(100) films. These results confirm the effect of impurities at the interfaces and were interpreted using a Time-Temperature-Transformation (TTT) diagram [15,16].

In Fig. 5, a similar TTT diagram is drawn for the Ni(10%Pt) case. In this diagram, the transformation curve of the amorphous phase into the crystalline phase (i.e., the temperature required for a thin layer to crystallize is plotted as a function of time) is represented with a dotted line. The “C” shape of this curve is due to two mechanisms governing the phase transformation. For low temperatures, the low mobility of the atoms limits the transformation of the amorphous phase into the crystalline phase: the kinetics factor is thus the main barrier to nucleation. On the other hand, for high temperatures, it is the thermodynamic factor that limits the nucleation since the nucleation barrier decreases with the driving force (the driving force becomes zero at the melting temperature). During a heat treatment (corresponding to a specific curve in the TTT diagram), the amorphous phase can continue to form as long as it does not meet the transformation curve. In Fig. 5, the curves in solid lines represent different heat treatments that have been performed for Ni(10%Pt) films on (100)Si substrate: the curves without points correspond to heat treatment for which the amorphous phase was found at the end of the heat treatment while, for the curves with points, the crystalline θ-Ni_2Si phase was reported. In Fig. 5, the transformation curve was modified to reproduce these experimental observations: i.e., the transformation curve should be above the curves corresponding to the heat treatments keeping the silicide in the amorphous state and should cut the curves corresponding to the heat treatments leading to a crystalline silicide.

The shape of the transformation curve was obtained by analyzing the kinetics of the amorphous-to-crystalline silicide transformation in terms of the classical theories of nucleation and growth [32–34] as detailed in Appendix C. Since large grains were found for the θ-Ni_2Si phase [11], the amorphous-to-crystalline silicide transformation was considered as a two-dimensional phase transformation process. In this case, the time to obtain a given volume fraction (f) of transformed Ni_2Si at a given temperature can be expressed by (see Appendix C for details):

$$t = \left(-\ln(1-f)\,/K(T)\right)^{1/3} \qquad \textit{Eq. 1}$$

where $K(T)$ depends only on the temperature and is given by:

$$K(T) = c_4 \left(\frac{\Delta G_V}{kT}\right)^2 exp\left(-\frac{c_2 \Delta\sigma^3 / \Delta G_V^2 + 3Q_g}{kT}\right) \quad \textit{Eq. 2}$$

With the c_4 constant is (Eq. A.8): $c_4 = \frac{\pi}{3}\,\Omega^2 n^{\frac{2}{3}}\, a_0^2\, \omega^3$

The Gibbs free energy change per unit volume of Ni_2Si, ΔG_V, can be approximated by [34]:

$$\Delta G_V = \frac{1}{\Omega}\frac{\mathrm{L}}{T_m}(T - T_m) \quad \textit{Eq. 3}$$

where $\Delta\sigma$ is the effective interfacial energy change accompanying nucleation, T_m is the melting point of the Ni_2Si phase, c_2 and c_4 are constants, L is the latent heat of fusion, Ω is the atomic volume and Q_g is the activation energy for atomic migration required during incoherent growth.

Eq. 1-3 were used to build the transformation curve in Fig. 5 by selecting the following parameters to usual values since their actual values are not known: $\Delta\sigma = 0.1\,J/m^2$ [34], $L/T_m = 10\,J/(mol.K)$ [35], and $Q_g = 0.8\,eV$ [28]. As the c_2 term should depend on several unknown interface energies, its value was chosen to the one for homogeneous nucleation site (i.e.: $c_2 = 16\pi/3$).The melting temperature was set to the congruent point for the θ-Ni_2Si phase (i.e. T=1306°C) in the Ni-Si phase diagram [36] since it is not known for the Ni-Pt-Si ternary phase diagram [37]. In Fig. 5, the c_4 constant was varied to fit the experimental data. From the expression of c_4 (Eq. A.8) and by taking $\omega = 10^{12}Hz$, $a_0 = 0.3\,nm$ and, $\Omega = 1\,10^{-29}m^3$, the number of nucleation site is found to be around $\mathrm{n} = 10^{22}m^{-3}$. This value corresponds to 10^{-7} time the number of atoms per unit volume ($= 1/\Omega$) and indicates that nucleation should occur at specific nucleation sites.

From the knowledge of the transformation curve in the TTT diagram, the heat treatment can be designed to obtain either the amorphous or the crystalline silicide. Indeed, amorphous phase can continue to form as long as it does not meet the transformation curve if the amount of metal (proportional to the thickness of the Ni(Pt) film) is sufficient. A maximum critical thickness for the formation of the amorphous can be thus defined depending on the heat treatment and the kinetics of the amorphous silicide formation. The TTT diagram drawn in Fig. 5 shows that the faster the rise in temperature is, the more the nucleation of the first silicide, at a given temperature, will take place from a greater thickness of amorphous silicide formed. In other words, the amorphous silicide will be more stable when the temperature rises rapidly, and the thickness of the silicide is small.

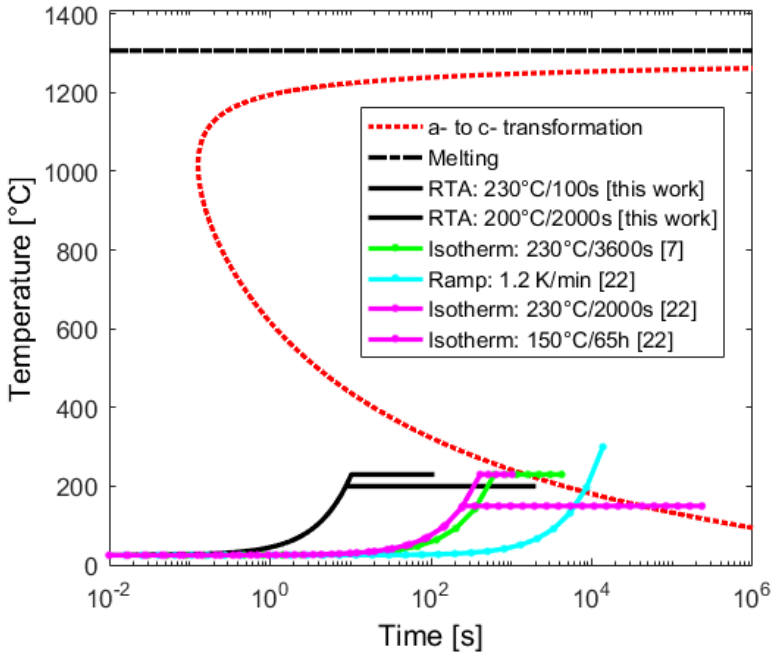

Fig. 5. *Schematic time-temperature-transformation (T-T-T) diagram for the nucleation and growth of θ-Ni_2Si crystalline phase starting from the amorphous phase (dotted line). The curves in solid lines represent different heat treatments that have been performed for Ni(10%Pt) films on (100)Si substrate: the curves without points correspond to heat treatment for which the amorphous phase was found at the end of the heat treatment while, for the curves with points [7,25] , the crystalline θ-Ni_2Si phase was reported.*

Thus, variations in the thermal budget (rate of temperature rise and/or temperature of the annealing stage) exert an influence on the nucleation of the first silicide. It is therefore more likely to observe the amorphous phase for RTA type annealing (short times and relatively high temperatures) than for in situ XRD annealing and/or conventional annealing which are longer and at relatively lower temperatures. This may explain the difference between previous studies based mainly on in-situ annealing where the θ-Ni_2Si phase was observed and our study where the amorphous phase is observed after RTA. This difference is also linked to the small thickness of metal deposited for the contacts (10 nm) that will be consumed by the growth of the amorphous phase before the critical thickness is reached. Consequently, the rapid thermal annealing (RTA) and the low thickness of metal deposited (total silicidation) or consumed (partial silicidation) used in our study lead to the growth of a first amorphous silicide and do not make it possible to obtain nucleation of the θ-Ni_2Si phase. Further experiments with thicker films and longer annealing together with TEM characterization could help to confirm this point but are beyond the goal of this paper.

The schematic diagram in Fig. 5 has been established from estimated parameters using the classical nucleation and growth law [33,34,38]. More complex models considering the specificities of the growth of the amorphous silicide such as diffusion asymmetry and/or the epitaxial growth of the θ-Ni_2Si

phase may lead to a better description of the TTT diagram. The effect of Pt on the parameters could also be more accurately considered. Indeed, Pt can have a thermodynamic effect by changing the driving forces of nucleation and/or growth of the amorphous and crystalline phases. It can also have a kinetics effect by changing the diffusion asymmetry in the amorphous phase, the kinetics barrier to the nucleation of the θ-Ni_2Si phase and/or the diffusion in θ-Ni_2Si. Other factors can also influence the formation of the amorphous as the first phase such as the presence of impurities linked to the surface preparation, the TiN encapsulation and the mechanical stresses which can also influence the kinetics and/or thermodynamics.

4.2. Kinetics of the amorphous Ni silicide

In our work, the first phase to grow is the amorphous silicide instead of θ-Ni_2Si whose kinetics has been studied previously [25,39]. As the kinetics of the amorphous silicide is not known, it's important to determine the law that defines the mechanisms and the parameters that govern its formation. Indeed, the thickness of the first phase formed in the RTA will determine the final thickness of the NiSi contact since the silicidation is partial during the RTA and the selective etch is used to remove the unreacted metal. Therefore, a good control of the salicide process requires the control of the growth rate of the amorphous phase.

In order to quantify and understand the variations in the growth kinetics of the amorphous silicide, several RTA were performed, and the thicknesses of the silicide were measured by XRR as a function of time for several temperatures for the reference sample without PAI as well as for the three different PAI samples (Fig. 3). This precise determination of the evolution of the silicide thickness will allow us comparing the experimental results to different growth models to determine the mechanisms linked to the growth of the first silicide during RTA. In the following, different growth models are thus confronted with our results to identify the mechanisms and to estimate the kinetics parameters which govern the growth of the amorphous silicide during an RTA for the reference sample and for the samples with PAI. The formation law that governs the growth of the first silicide is discussed by comparing the experimental results to the linear parabolic model, as well as a model considering nonlinear diffusion. The influence of the amorphous substrate is also discussed, and the silicide's kinetics are compared with literature.

The growth kinetics of the first silicide obtained by reaction between Ni films with a Pt content equal or superior to 10% Pt and a Si(100) substrate has been previously studied for samples without PAI [25,39]. Ehouarne et al.[39] studied the growth kinetics of the first silicide for 25 nm and 50 nm films of Ni(13%Pt) on Si(100). The kinetics of the first silicide was determined thanks to a combination of in-situ measurements based on XRD, XRR and Rs. These results were fitted by considering a growth limited by diffusion of Ni (Eq. B.11). Later, Panciera et al. [25] have studied the growth kinetics of the first silicide for an 11 nm thin film of Ni(10%Pt) deposited on Si(100). The kinetics of the first silicide was determined using in-situ XRD [25]. In these studies, the kinetics parameters were obtained by simulation of the XRD intensity of the metal alloy Ni(10%Pt)) assuming also a growth controlled by diffusion (Eq.

B.11). For these two studies, a growth controlled only by diffusion (Eq. B.11) was used for the simulations because the agreement between simulations and experimental results were close enough to neglect the reactions at the interfaces and thus the number of fitting parameters is reduced. These studies [25,39] have thus allowed to determine the kinetics parameters of growth of the first silicide for in situ measurements. However, they are based on total silicidation, and relatively large thermal budgets (due to in situ measurement) compared to the RTA used in the salicide process. The present study addresses the growth kinetics of the first silicide during partial silicidation and with RTAs at temperatures ranging from 200 to 230°C that correspond to the conditions used for the salicide process in the industry.

4.2.1.Linear-parabolic model

As discussed before, the model used by Ehouarne et al. [7,39] and Panciera [25] to fit the experimental results considers only diffusion through the silicide and neglects the reactions at the interfaces. However, the thickness evolution obtained in Fig. 4 cannot be simulated by this simple model since it appears to become more and more linear when the temperature increases (coefficient of determination R^2 is 0.90±0.02 for 200°C and 0.98±0.01 for 230°C). As the linear behavior is usually attributed to reactions at the interfaces, one should consider the reactions at the interfaces in the model in addition to the diffusion (for an isotherm, linear-parabolic model instead of the parabolic model). The linear-parabolic model or Deal and Grove law was initially established for the growth of oxides [40]. Nemouchi et al. [41] have shown that the growth of Ni silicides can be described by this model that takes into account the diffusion of Ni atoms as well as the reactions at the interfaces and gives a linear-parabolic law for an isotherm. Nemouchi et al. [41] have also shown that the activation energy for diffusion is larger than the ones for reaction leading to a more linear behavior at high temperatures compared to low temperatures. This finding seems to be in accordance with our results obtained by RTA (Fig. 4) for which a more linear behavior is observed with increasing annealing temperature. Thus, the Deal and Grove model seems to be a good candidate to describe the growth kinetics of the first silicide and to interpret the observed variations.

For isothermal annealing, the Deal and Grove model gives the linear-parabolic law:

$$\frac{L^2 - L_0^2}{2K_D} + \frac{L - L_0}{K_I} = t \qquad \textit{Eq. 4}$$

where K_D is the growth rate related to diffusion and K_I is the growth rate related to the reactions at the interfaces. L is the thickness of the phase. L_0 is the thickness of the silicide at the start of the annealing stage and thus corresponds to the silicide which is formed during the metal deposition or during the RTA temperature rise ramp. K_I and K_D are both the product of the variation of chemical potential across the growing phase ($\Delta\mu/k_BT$) and a kinetic term being the interface velocity (K) and the diffusion coefficient of the Ni atoms in the growing phase (D_{Ni}).

Eq. 4 can be rearranged to express the time as a second-degree polynomial of the thickness to fit the data more easily:

$$t = \frac{L^2}{2K_D} + \frac{L}{K_I} - \left(\frac{L_0^2}{2K_D} + \frac{L_0}{K_I}\right) \qquad \textit{Eq. 5}$$

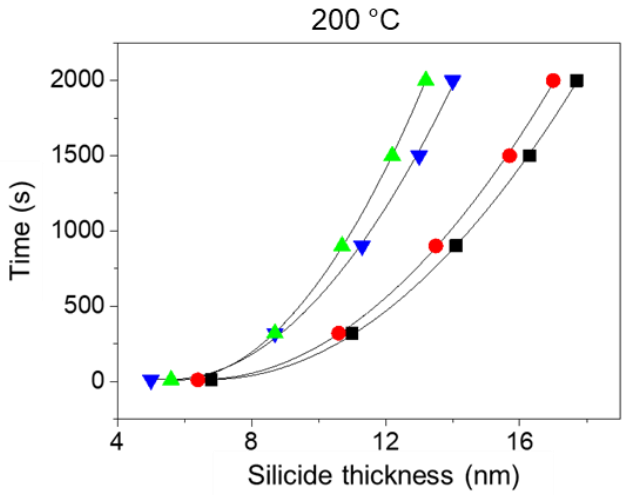

	A + BL + BL²		
	A	B	C
Q1	766	-223	16
Q2	754	-299	18
Q3	1167	-406	36
Q4	837	-299	27

Fig. 6. *Evolution of time as a function of silicide thickness for RTA annealing at 200°C. The symbols represent the experimental values, and the black lines represent the modeling of the experimental results by a second-degree polynomial. The coefficients A, B and C correspond to the coefficients of equation 5 which describes the evolution of the annealing duration as a function of the thickness of silicide formed by a second-degree polynomial.*

Fig. 6 illustrates the results of simulations with the linear-parabolic law for annealing at 200°C. The curves represent the modeling of the experimental results by a second-degree polynomial. The good agreement between the curves and the experimental points seems to indicate that the linear parabolic model describes well the phenomena involved during silicidation. However, the negative values of the coefficient B show that the results are not consistent (inconsistent values were also obtained for the other temperatures). Indeed, according to Eq. 5, the coefficient B is equal to the inverse of the growth rate linked to the reactions at the interfaces. This growth rate cannot physically correspond to a negative value. Similarly, the coefficient A; which depends on the initial silicide thickness (~nm) that is formed during the metal deposition and the anneal ramp induced to reach the rapid thermal anneal temperature (~13s); cannot correspond physically to a positive value. Thus, the simulation with the parabolic linear model is mathematically valid but physically inconsistent. Several simulation methods based on different expressions of the linear parabolic law have been tried but all of them lead to bad agreement with experimental results. Therefore, the model of growth by diffusion and reactions at the interfaces (Deal and Groove law) does not allow to describe our experimental results. In the work of Nemouchi et al. [40]

in which the linear parabolic model was successfully applied, thicker samples (50 nm of Ni) were studied, and longer annealing which induces a total consumption of the metal, while in our study, we use a 10 nm thick NiPt layer and RTA that induces a partial consumption of the metal.

4.2.2.Nonlinear reactive diffusion model

This finding led us to develop another model by considering the nonlinear diffusion induced by the strong gradient of chemical potential across the growing layer. Indeed, in our study, the growth takes place over a few nanometers because the thickness of the phase remains below 20 nm. This leads to large gradient in composition and/or chemical potential for which the linear diffusion assumption at the basis of the Deal and Groove law is no longer valid. Therefore, the nonlinear diffusion should be used [42,43]. More precisely (see details in the Appendix D), when diffusion is described by Nernst-Einstein's law, the atomic flux, J, is considered to be directly proportional to the driving force of diffusion (concentration gradient or chemical potential gradient) and is then referred to as linear diffusion [42,43]. On the other hand, when the diffusion distance is small and the concentration gradient is large, the diffusion can become nonlinear [42,43]. In the latter case, the nonlinear diffusion induces a nonlinear kinetic effect for the growth of one phase (Appendix D). In the case of a chemical driving force (i.e., gradient of chemical potential), the growth rate can be expressed as (see Appendix D):

$$\frac{dL}{dt} = 2\frac{D}{\lambda}\sinh\left[\frac{\lambda}{2kT}\frac{\Delta\mu}{L}\right] = a_{sh}sinh\left[\frac{b_{sh}}{L}\right] \qquad \textit{Eq. 6}$$

With λ the jump distance. The parameters a_{sh} and b_{sh} are defined as:

$$a = \frac{2D}{\lambda} \qquad \textit{Eq. 6.a}$$

$$b_{sh} = \frac{\lambda}{2}\frac{\Delta\mu}{kT} \qquad \textit{Eq. 6.b}$$

Note that Eq. 6 has been obtained by considering that a local equilibrium prevails at the interfaces of the growing phase. Under this assumption, the chemical potentials are fixed by the equilibria at the interfaces: therefore, $\Delta\mu$ is constant and the chemical potential gradient varies as the inverse of the phase thickness $\left(\frac{d\mu}{dz} \approx \frac{\Delta\mu}{L}\right)$. For relatively large thicknesses (i.e., when $L > b_{sh}$), the term inside the hyperbolic sine is small, and the limited development of $\sinh$ can be used:

$$\sinh[x] \approx x + \frac{x^3}{3!} \qquad \textit{Eq. 7}$$

Where $x = \frac{\lambda}{2kT}\frac{\Delta\mu}{L} = \frac{b_{sh}}{L}$

For larger thickness (L >> b_{sh}), Eq 7 becomes $\sinh[x] \approx x$ and the flux is proportional to the driving force (linear diffusion). The growth rate (dL/dt) can be expressed by:

$$\frac{dL}{dt} = D * \frac{\Delta\mu}{KT}\frac{1}{L} \qquad \textit{Eq. 8}$$

The integration of Eq. 8 classically leads to a thickness proportional to the root of time, which corresponds to the parabolic law (Eq. 9):

$$LdL = a_l dt \Rightarrow L^2 - L_0^2 = \frac{K_D}{2}t = D\frac{\Delta\mu}{2kT}t \Rightarrow L \propto t^{1/2} \qquad \textit{Eq. 9}$$

When the thicknesses are smaller, the linear approximation is not valid anymore and the x^3 term is required. The growth rate is thus generally given by Eq. 6 but can also be approximated by:

$$\frac{dL}{dt} = D\left(\frac{\Delta\mu}{kT}\frac{1}{L} + \frac{\lambda^2}{24}\left(\frac{\Delta\mu}{kT}\right)^3\frac{1}{L^3}\right) = \frac{K_D}{L} + \frac{b_{nl}}{L^3} \qquad \textit{Eq. 10}$$

Where b_{nl} corresponds to the kinetic coefficient of the nonlinear approximation

It should be emphasized that Eq. 6 is the more general law and that Eq. 9 and 10 are only approximations of Eq. 6. Thereafter, Eq. 6 will be called “nonlinear reactive diffusion law” while Eq. 9 and Eq. 10 will be called linear approximation and nonlinear approximation respectively. Whereas the equations for nonlinear diffusion (Eq. B.12 to B.16) are well established [42,43], the application to phase growth by reactive diffusion (Eq. 6) has not been previously established to our knowledge.

To determine the validity of the linear and nonlinear approximation, the experimental thicknesses for the reference sample. after RTA at 200°C have been fitted by Eq. 6 (nonlinear reactive diffusion law), Eq. 9 (linear approximation) and Eq. 10 (nonlinear approximation) in Fig. 7.a. The parabolic law (linear approximation) is not fitting the data well while the good match with Eq. 6 and 10 indicates that the nonlinear reactive diffusion law should be applied either through the sinh variation (Eq. 6) or through the approximation (Eq. 10).

The nonlinear reactive diffusion law (Eq. 6) with the sinh is more general than its approximations and should thus be preferably chosen for the fit. However, the approximations (Eq. 9 and 10) are simpler and can be integrated to have analytical expressions for the phase thickness as a function of time (see Appendix D). It is thus interesting to estimate the validity of the approximations to describe the sinh function.

In Fig. 7.b, the variation of $sinh[b_{sh}/L]$ as a function of the thickness is compared to the two approximations of the $sinh[b_{sh}/L]$: i.e. the linear approximation (first order) and the nonlinear approximation (3rd order, Eq.7), The value of b_{sh} was taken to be 25 nm from the fit with Eq. 6 of the reference sample annealed at 200°C (Fig. 7.a). For thicknesses below 15 nm, there is a significant difference between $sinh[b_{sh}/L]$ and its approximations. This difference is very large for the linear approximation but is also large for the nonlinear approximation. Therefore, the two approximations cannot be used to describe the kinetics of the silicide growth and the fit will be performed with Eq. 6 ($sinh[b_{sh}/L]$) in the following.

Fig. 7.b shows that the nonlinear reactive diffusion law (Eq. 6) should be taken for thicknesses lower than 15 nm. This is in accordance with the b_{sh} value of 25 nm since for thicknesses larger than 25 nm, x will be smaller than 1 and therefore the approximations (Eq. 7) start to be valid. For thicknesses much larger than b_{sh}, the parabolic law can be applied for the silicide growth. Note that the b_{sh} value should depend on the nature of the silicide since the variation of chemical potential and the diffusion distance depend on the silicide.

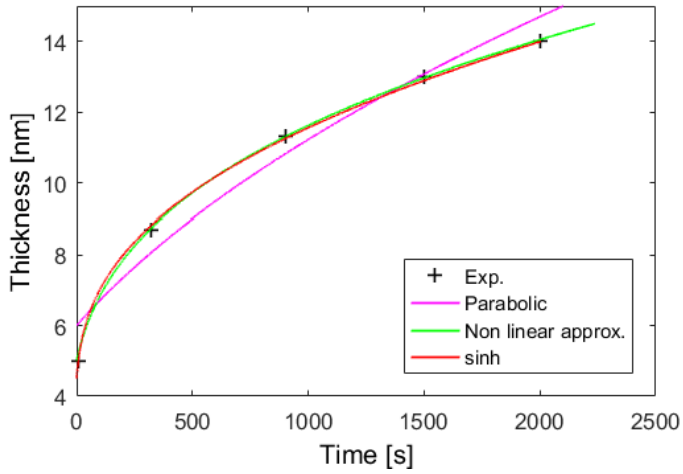

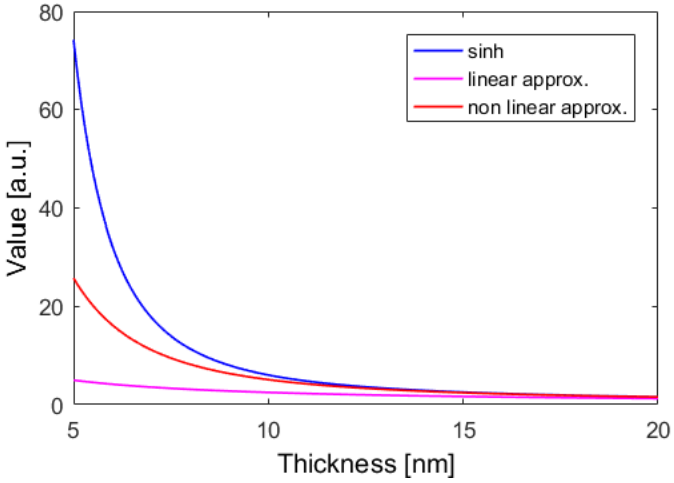

Fig. 7. (a) Fit of the experimental thickness for RTA annealing at 200°C of the reference sample Using Eq. 6 (nonlinear reactive diffusion law), Eq.9 (linear approximation) and, Eq.10 (nonlinear approximation). The symbols represent experimental values. (b) Comparison of the sinh function (blue curve) using the value of b_{sh} obtained in (a) with the one term expansion (magenta curve) and the two terms expansion (red curve) in Eq. 7.

Nonlinear reactive diffusion model for the reference sample

The experimental data for the different RTA annealing of the reference samples and the samples with the three PAI conditions were thus fitted by simulation with the nonlinear reactive diffusion law (Eq. 6). Fig. 8 shows the simulations performed for the reference sample without PAI. The experimental results represented with the red symbols, correspond to the silicide thickness measured by XRR as a function of time for several temperatures. The simulations represented with the blue lines show the very good agreement between the experimental values and the nonlinear reactive diffusion model.

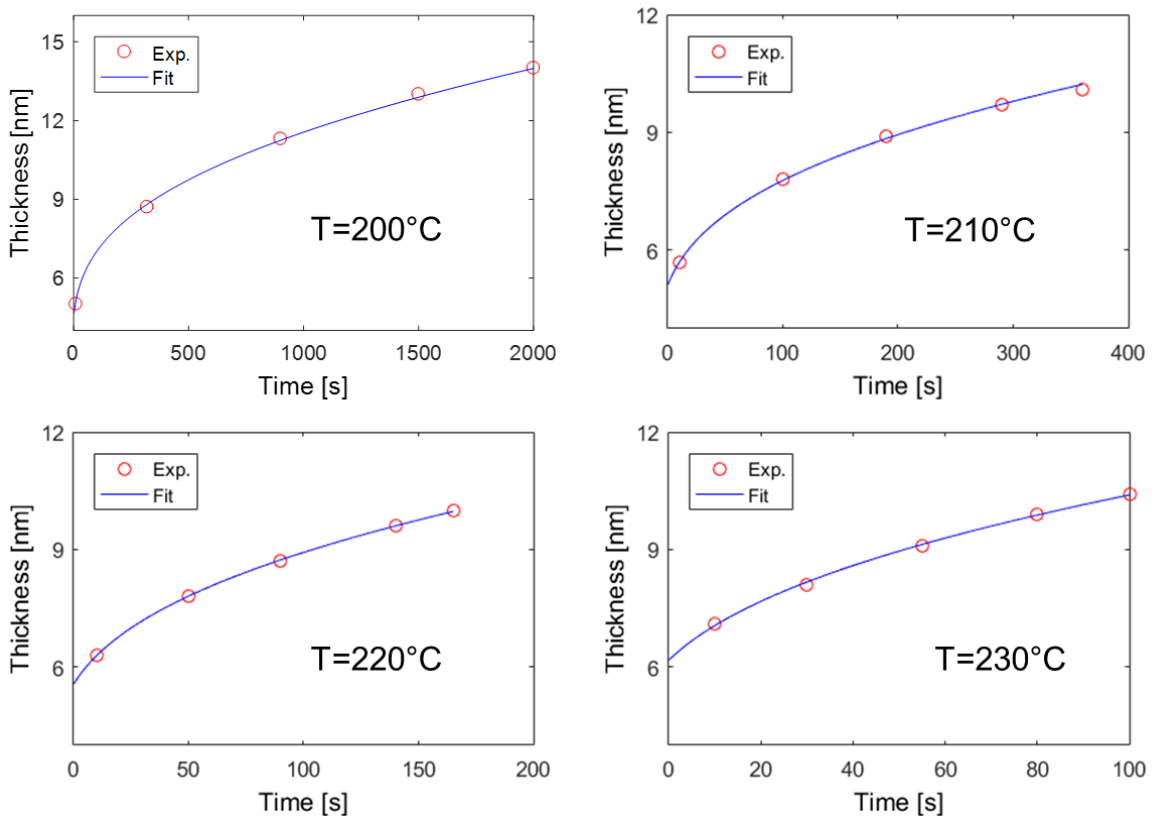

Fig. 8. Simulation with the nonlinear reactive diffusion model of the evolution of the silicide thickness as a function of time for several temperatures of the RTA obtained experimentally for the reference sample without PAI.

Table 1. Parameters (a_{sh}, b_{sh}, L_0) obtained from the fit using Eq. 6 of the experimental results obtained for the reference sample without PAI. For the b_{sh} parameter, the fit was performed for the RTA at 200°C and was modified to consider the variation of temperature: $b_{sh}(T)=473/T\ b_{sh}(200°C)$ where T is the temperature in K. The last column gives the coefficient of determination, R^2. The errors for a_{sh} and L_0 are ±2%.

T [°C]	a_{sh} [nm/s]	b_{sh} [nm]	L_0 [nm]	R^2
200	0 .000702	25	4 .5	0 .9992
210	0 .00125	24 .5	5 .1	0 .9985
220	0 .00255	24	5 .5	0 .9997
230	0 .0051	23 .5	6 .2	0 .9989

Table 1 shows the parameters (a_{sh} , b_{sh}, L_0) resulting from the fit with Eq. 6 of the experimental results obtained for the reference sample without PAI. The coefficients of determination (last column) are all larger than 0.99 showing the good fit. The initial thickness of the silicide (L0), which corresponds to the silicide thickness formed during the metal deposition and annealing ramping of the RTA, is coherent since it increases with the thermal budget (the annealing ramp to reach the temperature of annealing induces that the thermal budget increases with the temperature). For RTAs at 200°C (473K), the best fit is obtained for a b_{sh} value equal to 25±2 nm. For the other temperatures, Eq. 6.a can be used to calculate b_{sh} using the following relationship $b_{sh}(T)/b_{sh}(473K) = 473/T$ since $\Delta\mu$ and λ should be independent from T. Eq. 6.a also shows that b_{sh} is proportional to $\Delta\mu/kT$. Although $\Delta\mu/kT$ is not known for the amorphous silicide, it can be estimated to be around 23 [44]. From this estimation and the value $b_{sh}(473K) = 25\ nm$, one obtains, through Eq. 6.a, a diffusion distance, λ, of around 2.1 nm. This value is relatively high compared to the usual distance between atoms and indicates that the fitted b_{sh} is larger than expected. This may be due to a complex diffusion mechanism in the amorphous silicide since diffusion in an amorphous phase may involve thermally activated, highly collective atomic processes [45]. Another reason for this high value of b_{sh} may be a complex variation of the chemical potential due to the gradient of composition in the amorphous silicide [43].

Eq. 6.a shows that the other fitting parameter, a_{sh} , is the product of λ and D . The value of λ has been already discussed above and might be overestimated. However, the product $a_{sh}b_{sh}$ is interesting since it is equal to the effective diffusion coefficient [46] and allows to eliminate λ:

$$D_e = a_{sh}b_{sh} = D\frac{\Delta\mu}{kT} = K_D \qquad \textit{Eq. 11}$$

where D is the Nernst-Einstein diffusion coefficient [46], $\Delta\mu$/kT the thermodynamic factor, and K_D is the parabolic growth rate, (Eq. 9). In the following, for the sake of simplicity, the effective diffusion

coefficient will be called diffusion coefficient while D will be explicitly named Nernst-Einstein diffusion coefficient.

Eq. 11 shows that the effective diffusion coefficient is also equal to K_D [46] and thus allows to compare with the literature. Indeed, the usual laws used to fit the kinetics of silicide formation are the parabolic or linear-parabolic laws that determine K_D.

Table 2 summarizes the diffusion coefficients obtained for the reference sample as a function of annealing temperatures. The values obtained are consistent with each other since the coefficients increase with temperature. The values of the PAI samples are also reported in Table 2 and will be compared with each other and with the reference sample.

Effect of the PAI on the kinetics parameters

Table 2. Effective diffusion coefficients (Eq. 11) in nm^2/s obtained for the different conditions of PAI and annealing temperatures. The errors for D_e are ±2%.

T [°C]	200	210	220	230
D_e (Q1) [nm^2/s]: Ge PAI $1x10^{14}$ 20k	$1.9x10^{-2}$	$4.0x10^{-2}$	$7.5x10^{-2}$	$1.3x10^{-1}$
D_e (Q2) [nm^2/s]: Ge PAI $9x10^{14}$ 13k	$1.7x10^{-2}$	$3.3x10^{-2}$	$6.2x10^{-2}$	$1.2x10^{-1}$
D_e (Q3) [nm^2/s] : Ge PAI $9x10^{14}$ 13k and C PAI $4x10^{15}$ 3k	$6.7x10^{-3}$	$1.4x10^{-2}$	$2.5x10^{-2}$	$5.0x10^{-2}$
D_e (Q4) [nm^2/s]: Reference (without PAI)	$8.9x10^{-3}$	$1.5x10^{-2}$	$2.7x10^{-2}$	$5.0x10^{-2}$

Similar to the reference sample, a very good agreement with the experimental values is reached by Eq.6 for the three other samples: Q1, Q2 and Q3. Indeed, the coefficient of determination, R^2, is greater than 0.99 for all the adjustments and greater than 0.999 for most of them. This agreement allows extracting a coherent diffusion coefficient for each sample. Table 2 shows that the samples with Ge PAI (Q1 and Q2) have a greater diffusion coefficient than the ones of the reference sample without PAI and the samples with co-implantation of Ge and C.

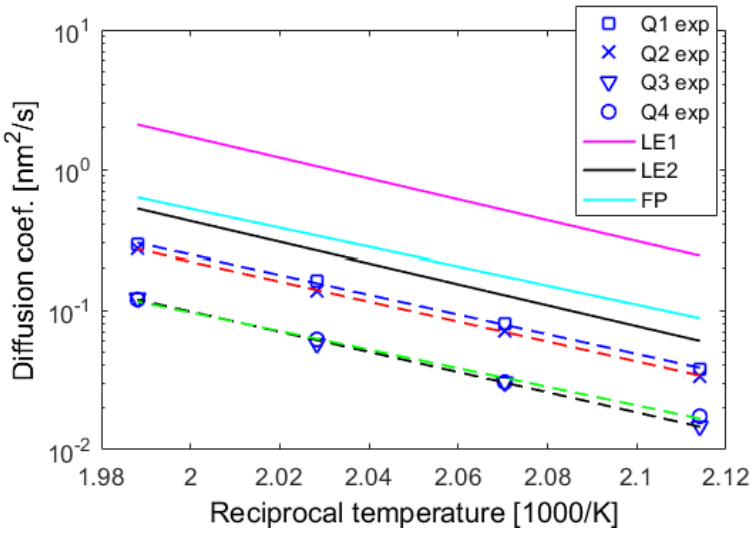

Fig. 9. Arrhenius diagram for the effective diffusion coefficients as a function of the inverse of the temperature for the samples with PAI: Q1 = PAI Ge 1x10^{14} 20k; Q2 = PAI Ge 9x10^{14} 13k; Q3 = PAI Ge 9x10^{14} 13k + PAI C 4x10^{15} 3k; as well as for the reference samples without PAI (Q4). For comparison, the values from previous works are also reported: LE1 = Ehouarne et al, 50 nm [39]; LE2 = Ehouarne et al, 25 nm [39]; FP = Panciera [25].

Moreover, the coherence of the fit is reinforced by Fig. 9 which presents the Arrhenius diagrams for the diffusion coefficients for the three samples with PAI (Q1, Q2, Q3) and for the reference sample without PAI. Indeed, the experimental values follow an Arrhenius behavior which makes it possible to determine the activation energy for the three PAI conditions and the reference sample without PAI**.**

Table 3 summarizes the kinetics parameters (pre-exponential factor and activation energy) obtained for each sample. The kinetics parameters of the samples with PAI differ from those of the reference sample without PAI. For the samples with PAI, the pre-exponential factor and the activation energy are greater than for the reference sample without PAI. This result shows that the growth kinetics of the first silicide in contact with an amorphous substrate differs from those in contact with a crystalline substrate. A similar effect was obtained by Delwail et al [24] that shows an increase of the silicide thickness for Ge PAI samples. Those results were obtained by comparing the influence of different Ge PAIs after the salicide process. Eq. 11 shows that the effective diffusion coefficient (Fig. 9 and Table 2) contains two terms: the self-diffusion coefficient D, and the thermodynamic factor $\Delta\mu/kT$. Delwail et al [24] have estimated the difference of the thermodynamic factor (difference of $\Delta\mu$) for the formation of the first phase from an amorphous or a crystalline Si substrate (a-Si and c-Si). Since the free energy of a-Si is greater than the free energy of c-Si, the estimated driving force ($\Delta\mu$) for the growth of amorphous silicide is greater by about 35% when in contact with a-Si (- 110 kJ/at.gram) than with c-Si (- 85 kJ/at.gram). Note that Delwail et al [24] have reported the values of the Gibbs free energy of the formation instead of $\Delta\mu$. If the driving force is greater for the samples having an a-Si substrate, the effective diffusion coefficient will be higher for these samples.

However, Table 1 shows that the diffusion coefficient is about 2 times higher for the Ge PAI samples than for the reference. Therefore, the change in driving force cannot fully explain the increase in growth rate. In addition to the driving force or thermodynamic factor, the effective diffusion coefficient (and the growth rate) of the first silicide also depends on the self-diffusion coefficient (Eq. 11). In the case of Ni silicides, it has been shown that Ni is the dominant diffusing species during silicidation [47]. Ni is also expected to be the main diffusion species in the amorphous silicide [48]. The Ni self-diffusion coefficient in the amorphous silicide may be influenced by several factors. The change in equilibrium (a-Si versus c-Si) may change the amorphous silicide composition and thus its integrated diffusion coefficient. D can also be increased by the presence of Ge since the growth kinetics of the Ni germanides were found to be faster than the ones of the Ni silicides [49]. The PAI conditions and, in particular, the Ge fluence may also influence the nature of the a-Si and possibly modify the self-diffusion coefficient [45].

The sample with Ge+C PAI induces effective diffusion coefficients almost equal to those of the reference sample and thus smaller than those obtained with Ge PAI. Therefore, the Ge+C PAI sample slows down the rate of formation of the silicide and cancels the effect of the Ge PAI. This effect can be of chemical nature by changing the driving force for the phase growth and/or the diffusion. However, the addition of carbon increases the quantity of atoms (Ge and C) implanted in Si, so there could also be a physical effect related to the concentration of atoms implanted independently of their nature. It has been argued that carbon atoms can segregate at the grain boundary and slows down the diffusion of Ni [50]. This effect cannot operate in amorphous phase since there are no grain boundaries. However, the carbon atoms could accumulate at the silicide/Si interface if they do not incorporate into the silicide. This could slow down the progression of the growth front by decreasing the interface velocity and/or the diffusion.

Table 3. Kinetics constants of the normal growth of the first silicide obtained with the nonlinear model for the three samples with PAI (Q1, Q2, Q3) as well as the reference sample without PAI (Q4). The values from Ehouarne et al. [7,39] and Panciera et al. [25] obtained by the parabolic law are also reported. The sample characteristics and the experimental conditions are given.

Film	Metal thickness (nm)	PAI	Thermal budget	Pre-exponential factor (cm^2/s)	Activation energy (eV)	Ref
Ni(10%Pt)	10	Q1: PAI Ge $1x10^{14}$ 20k	RTA, 200-230°C	0.31	1.40	this work
Ni(10%Pt)	10	Q2: PAI Ge $9x10^{14}$ 13k	RTA, 200-230°C	0.40	1.41	this work
Ni(10%Pt)	10	Q3: PAI Ge $9x10^{14}$ 13k and PAI C $4x10^{15}$ 3k	RTA, 200-230°C	0.29	1.44	this work

Ni(10%Pt)	10	Q4: none	RTA, 200-230°C	0.021	1.32	this work
Ni(13%Pt)	50	None	Isotherms 220°C and 270°C Rampes 5°C/min	14	1.48	[39]
Ni(13%Pt)	25	None	Isotherms 195 and 270°C Rampes 3 and 25 °C/min	3.5	1.48	[39]
Ni(10%Pt)	11	None	Isotherms 150°C up to 230°C	0.21	1.35	[25]

Comparison of the kinetics parameters with literature

To compare with former results, the effective diffusion coefficients determined for Ni(13%Pt)/Si(100) [7,39] and Ni(10%Pt)/Si(100) [25] are also reported in Table3 and Fig. 9. The diffusion coefficients are lower for our samples than those reported previously [7,25,39].The values reported from the literature consider only the diffusion through the growing silicide since the interface reactions are negligible for larger thicknesses. Therefore, the difference could be due to the models used but the two models should be equivalent for relatively large thicknesses. Nevertheless, the greatest contribution to this difference undoubtedly come from the nature of the silicide: amorphous for our study and crystalline in the literature [7,25,39]. Indeed, the two terms entering in the effective diffusion coefficient (self-diffusion coefficient D, and thermodynamic factor $\Delta\mu/kT$) should depend on the amorphous or crystalline nature of the growing phase. The thermodynamic factor for the first phase is proportional to the Gibbs free energy of formation of that phase: as the amorphous silicide is metastable, it should be smaller for the amorphous silicide than for the crystalline silicide. The Nernst-Einstein self-diffusion coefficient should also be different in the amorphous and crystalline silicide but it is difficult to know which one is the higher considering that grain boundary diffusion is dominant in crystalline thin films [47] while only bulk diffusion should be acting in an amorphous phase.

Application for microelectronics contacts

On a more industrial consideration, it is important to know the kinetics of the first silicide for the salicide process since it not only determines the thickness of the silicide after the first RTA (RTA1) but also the final silicide thickness after the second RTA (RTA2) as the selective etch between RTA1 and RTA2 removes the unreacted metal. To control the salicide process, the knowledge of the kinetics law is thus crucial, and the nonlinear reactive diffusion law gives quite a different behavior from the linear parabolic law. The former seems to be related to the amorphous silicide layer while the latter could be appropriated

for crystalline phases. The formation of amorphous or crystalline silicide could thus lead to different thickness of NiSi.

In conditions leading to the formation of the amorphous silicide, the nonlinear reactive diffusion law should be used to determine the silicide thickness after RTA1 at least if its thickness is small . It is thus important to know when the nonlinear reactive diffusion law must be used. A numerical evaluation of $\sinh(x)$ and its expansion (Eq. 7) has been performed and shows that the linear approximation and the nonlinear approximation differs by 10% of the $\sinh(x)$ for $x{\sim}0.75$ and $x{\sim}2$ respectively. It means that the parabolic law should be valid for $L > \frac{3}{2} b_{sh}$. For the amorphous silicide with b_{sh} around 25 nm, this means $L > 40\ nm$. On the other hand, the nonlinear reactive diffusion law must be used for $L < \frac{b_{sh}}{2}$, this means $L < 12.5\ nm$ for the amorphous silicide (since the nonlinear approximation differs by more than 10%).

However, as already discussed above, b_{sh} should depend on the growing phase and may be smaller for crystalline phase. Since b_{sh} is not known 'a priori', it might be useful to have a practical way to determine if the nonlinear reactive diffusion law should be applied. Annex B shows that the nonlinear approximation can lead to a thickness proportional to time at the fourth root (Eq. B.22 and Eq. 12):

$$L^4 - L_0^4 = \frac{b_{nl}}{4} t \Rightarrow L \propto t^{1/4} \qquad \textit{Eq. 12}$$

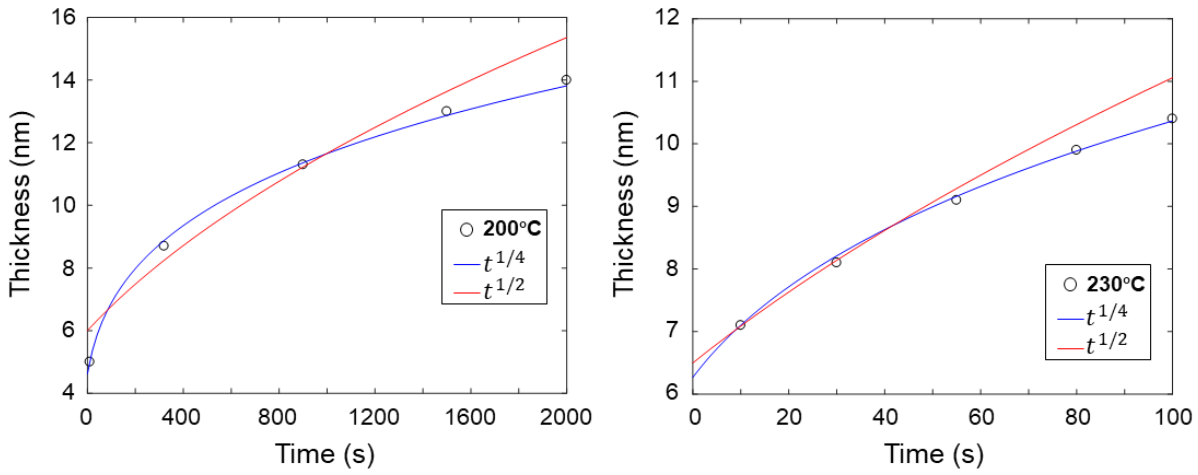

Fig. 10. *Fit of the experimental silicide thickness for RTA annealing at 200°C and 230°C of the reference sample. The symbols represent experimental values. The red and blue lines correspond to a fit with $t^{1/2}$ (Eq. 8) and $t^{1/4}$ (Eq. 12) respectively.*

Fig. 10 shows the fit of the experimental thicknesses by Eq. 8 and Eq. 12 for the reference sample. The closer match with the $t^{1/4}$ dependency indicates that this dependency can be used to reveal the

nonlinear reactive diffusion. However, this $t^{1/4}$ dependency is only a rough approximation and the parameters deduced from the fit (b_{nl}) can be substantially different from the one determined using Eq. 6.

For crystalline phases, b_{sh} may be smaller and, thus more difficult to measure. Moreover, for crystalline phases, the growth can be not planar and thus the nonlinear reactive diffusion may not be relevant. Indeed, crystalline phases (e.g. θ-Ni_2Si) usually nucleate first and then grow laterally [28]. As these two growth steps occur usually over a thickness of about 10 nm [28], the nonlinear reactive diffusion cannot be applied and observed for these first 10 nm on which it should have the strongest effect. For amorphous silicide, there is neither nucleation nor lateral growth since it already forms during the deposition. That could explain why we were able to observe the nonlinear reactive diffusion in our work while it may be difficult for the crystalline silicide due to a smaller b_{sh} and to the nucleation/lateral growth.

Furthermore, for the industry, besides the problem with agglomeration, the variation in phase sequence has been an aggravating source of difficulty. In the Ni-Si system, the presence of multiple metal-rich phases often ensures a variable and complex path to the monosilicide. The last phase present before NiSi determines the energy available for the formation of NiSi, affects the formation temperature and can bring in important nucleation effects, if that energy is too small. Different substrates and preparation conditions will thus lead to different phase sequences and different formation temperatures for the monosilicide. Because a microelectronic wafer represents multiple substrates, as each of the source and drain regions can be Si, SiGe (sometimes Si(C)) with variable dopant types and concentration in each (n, p regions and at times undoped regions or even n+p regions depending on design), the phase sequence varies with the regions of a chip and the process needs to be optimized for all regions simultaneously. This was one of the biggest engineering challenges of this material set. The process optimization is further complicated by possible variation in cleaning steps, in queue time before deposition, in in-situ cleans before metal deposition and, importantly, in deposition parameters during sputtering. Fortunately, the addition of 10% Pt in the Ni film appears to lead to more uniform NiSi growth on the different part of the wafer. In this case, the first phase to grow is either the amorphous silicide or θ-Ni2Si. These two phases, although having a different structure, are similar for some points: they are non-stochiometric with a similar range in Ni/Si concentration and they seem to easily incorporate elements such as Pt, W, Ge. The better behavior of the Ni(10%Pt) silicidation might thus be related to extended solubility of elements (Ge, dopants) contained in the substrate. The incorporation of these elements could also favor the growth of the amorphous silicide as Pt is doing. Furthermore, the growth competition between amorphous silicide and θ-Ni_2Si could be due to relative similar formation energies leading to a similar driving force for NiSi nucleation. However, the final properties of NiSi contacts, such as agglomeration, roughness, electrical resistance, could also depend on the structure, microstructure, and texture of the first phase.

5. Conclusion

In this work, the nature and the growth kinetics of the first silicide obtained during the solid-state reaction between a 10 nm Ni0.9Pt0.1 film and a Si substrate have been studied for heat treatments by RTA similar to the ones used for the salicide process. The effect of the amorphization of the Si substrate has also been examined for three different PAI conditions to be compared to the reference sample without PAI.

The first silicide to grow is amorphous for all our samples in contrast with previous studies based on similar Pt percentage and NiPt thickness for which the first silicide is the crystalline θ-Ni2Si phase. Several aspects related to the processes used during the silicidation were considered to explain this difference: the thickness of consumed metal and the use of RTA appear to be the main factors that inhibit the nucleation and growth of the θ-Ni2Si phase. A TTT diagram allows comparing the influence of the thermal anneals used in this study and former ones as well as pointing out the influence of our RTAs on the inhibition of the silicide's crystallization.

The silicide thickness of this amorphous silicide has been determined by XRR after each RTA to obtain the kinetics of the silicide formation for each sample at four temperatures. In order to quantify and identify the mechanisms of formation, the silicide kinetics was firstly modelized with the linear parabolic model, but non-physical parameters were obtained for all samples and all temperatures.

This result is attributed to the nanometric thicknesses (< 18 nm) of the amorphous silicide that lead to strong gradient of driving force (chemical potential). To consider these nanometric thicknesses and strong driving forces, a nonlinear reactive diffusion model is developed in which the growth rate is proportional to the hyperbolic sinus of the gradient of chemical potential. This behavior reflects the influence of the nonlinear effects related to the strong gradient of chemical potential due to the small silicide thickness.

The nonlinear reactive diffusion model allows us to determine the effective diffusion coefficient and its activation energy for each sample. The differences in effective diffusion coefficients (and activation energy) provide some understanding of the PAI influence on the growth kinetics of the silicidation process. The influence of the amorphous substrate on the silicide growth is discussed qualitatively and quantitatively. The Ge PAI has an accelerating effect on the silicide formation that could be related to thermodynamic (driving force) but also kinetics (self-diffusion coefficient). However, the Ge+C PAI seems to cancel the influence of the Ge PAI.

Compared to previous works, the effective diffusion coefficients are lower for our samples than those reported previously. The greatest contribution to this difference comes certainly from the nature of the phase: amorphous for our study and crystalline in former studies. The validity and applicability of the nonlinear reactive diffusion, considering the application for microelectronics contacts, are also discussed.

Acknowledgments

Denis Marseilhan from CEA/LETI is acknowledged for performing RTA. The authors thank Magali Grégoire from STMicroelectronics as well as Pierre Benigni, Christophe Girardeaux from IM2NP for

fruitful discussions. The reviewers are greatly acknowledged for their nice suggestions that were included in the paper.

References

[1] C. Lavoie, F.M. d'Heurle, C. Detavernier, C. Cabral Jr., Towards implementation of a nickel silicide process for CMOS technologies, Microelectronic Engineering. 70 (2003) 144–157. https://doi.org/10.1016/S0167-9317(03)00380-0.

[2] D. Mangelinck, J.Y. Dai, J.S. Pan, S.K. Lahiri, Enhancement of thermal stability of NiSi films on (100)Si and (111)Si by Pt addition, Applied Physics Letters. 75 (1999) 1736–1738. https://doi.org/10.1063/1.124803.

[3] C. Detavernier, C. Lavoie, Influence of Pt addition on the texture of NiSi on Si(001), Applied Physics Letters. 84 (2004) 3549. https://doi.org/10.1063/1.1719276.

[4] T. Sonehara, A. Hokazono, H. Akutsu, T. Sasaki, H. Uchida, M. Tomita, H. Tsujii, S. Kawanaka, S. Inaba, Y. Toyoshima, Contact resistance reduction of Pt-incorporated NiSi for continuous CMOS scaling ~ Atomic level analysis of Pt/B/As distribution within silicide films ~, in: 2008 IEEE International Electron Devices Meeting, 2008: pp. 1–4. https://doi.org/10.1109/IEDM.2008.4796851.

[5] O. Weber, E. Josse, F. Andrieu, A. Cros, E. Richard, P. Perreau, E. Baylac, N. Degors, C. Gallon, E. Perrin, S. Chhun, E. Petitprez, S. Delmedico, J. Simon, G. Druais, S. Lasserre, J. Mazurier, N. Guillot, E. Bernard, R. Bianchini, L. Parmigiani, X. Gerard, C. Pribat, O. Gourhant, F. Abbate, C. Gaumer, V. Beugin, P. Gouraud, P. Maury, S. Lagrasta, D. Barge, N. Loubet, R. Beneyton, D. Benoit, S. Zoll, J.-D. Chapon, L. Babaud, M. Bidaud, M. Gregoire, C. Monget, B. Le-Gratiet, P. Brun, M. Mellier, A. Pofelski, L.R. Clement, R. Bingert, S. Puget, J.-F. Kruck, D. Hoguet, P. Scheer, T. Poiroux, J.-P. Manceau, M. Rafik, D. Rideau, M.-A. Jaud, J. Lacord, F. Monsieur, L. Grenouillet, M. Vinet, Q. Liu, B. Doris, M. Celik, S.P. Fetterolf, O. Faynot, M. Haond, 14nm FDSOI technology for high speed and energy efficient applications, in: 2014 Symposium on VLSI Technology (VLSI-Technology): Digest of Technical Papers, 2014: pp. 1–2. https://doi.org/10.1109/VLSIT.2014.6894343.

[6] C. Lavoie, C. Detavernier, C. Cabral Jr., F.M. d'Heurle, A.J. Kellock, J. Jordan-Sweet, J.M.E. Harper, Effects of additive elements on the phase formation and morphological stability of nickel monosilicide films, Microelectronic Engineering. 83 (2006) 2042–2054. https://doi.org/10.1016/j.mee.2006.09.006.

[7] M. Putero, L. Ehouarne, E. Ziegler, D. Mangelinck, First silicide formed by reaction of Ni(13%Pt) films with Si(1 0 0): Nature and kinetics by in-situ X-ray reflectivity and diffraction, Scripta Materialia. 63 (2010) 24–27. https://doi.org/10.1016/j.scriptamat.2010.02.040.

[8] J. Demeulemeester, D. Smeets, C.M. Comrie, C. Van Bockstael, W. Knaepen, C. Detavernier, K. Temst, A. Vantomme, The influence of Pt redistribution on Ni(1-x)Pt(x)Si growth properties, Journal of Applied Physics. 108 (2010) 043505. https://doi.org/10.1063/1.3455873.

[9] J. Demeulemeester, D. Smeets, C.M. Comrie, N.P. Barradas, A. Vieira, C. Van Bockstael, C. Detavernier, K. Temst, A. Vantomme, On the growth kinetics of Ni(Pt) silicide thin films, Journal of Applied Physics. 113 (2013) 163504. https://doi.org/10.1063/1.4802738.

[10] F. Panciera, K. Hoummada, C. Perrin, M. El Kousseifi, R. Pantel, M. Descoins, M. Gregoire, M. Juhel, D. Mangelinck, Ni(Pt)-silicide contacts on CMOS devices: Impact of substrate nature and Pt concentration on the phase formation, Microelectronic Engineering. 120 (2014) 34–40. https://doi.org/10.1016/j.mee.2013.12.016.

[11] F. Panciera, D. Mangelinck, K. Hoummada, M. Texier, M. Bertoglio, A. De Luca, M. Gregoire, M. Juhel, Direct epitaxial growth of θ-Ni2Si by reaction of a thin Ni(10 at.% Pt) film with Si(1 0 0) substrate, Scripta Materialia. 78–79 (2014) 9–12. https://doi.org/10.1016/j.scriptamat.2014.01.010.

[12] M. El Kousseifi, K. Hoummada, M. Bertoglio, D. Mangelinck, Selection of the first Ni silicide phase by controlling the Pt incorporation in the intermixed layer, Acta Materialia. 106 (2016) 193–198. https://doi.org/10.1016/j.actamat.2016.01.004.

[13] F.A. Geenen, E. Solano, J. Jordan-Sweet, C. Lavoie, C. Mocuta, C. Detavernier, The influence of alloying on the phase formation sequence of ultra-thin nickel silicide films and on the inheritance of texture, Journal of Applied Physics. 123 (2018) 185302. https://doi.org/10.1063/1.5022070.

[14] D. Mangelinck, M. El Kousseifi, K. Hoummada, F. Panciera, T. Epicier, Lateral growth of NiSi at the θ-Ni2Si/Si(100) interface: Experiments and modelling, Microelectronic Engineering. 199 (2018) 45–51. https://doi.org/10.1016/j.mee.2018.07.014.
[15] K. van Stiphout, F.A. Geenen, N.M. Santos, S.M.C. Miranda, V. Joly, J. Demeulemeester, C. Mocuta, C.M. Comrie, C. Detavernier, L.M.C. Pereira, K. Temst, A. Vantomme, Ion beam modification of the Ni-Si solid-phase reaction: The influence of substrate damage and nitrogen impurities introduced by ion implantation, J. Phys. D: Appl. Phys. 54 (2020) 015307. https://doi.org/10.1088/1361-6463/abb046.
[16] K. van Stiphout, F.A. Geenen, N.M. Santos, S.M.C. Miranda, V. Joly, J. Demeulemeester, C. Detavernier, F. Kremer, L.M.C. Pereira, K. Temst, A. Vantomme, Impurity-enhanced solid-state amorphization: the Ni–Si thin film reaction altered by nitrogen, J. Phys. D: Appl. Phys. 52 (2019) 145301. https://doi.org/10.1088/1361-6463/ab00d2.
[17] S. Guillemin, P. Gergaud, N. Bernier, L. Lachal, F. Mazen, A. Jannaud, F. Nemouchi, Ph. Rodriguez, Influence of dual Ge/C pre-amorphization implantation on the Ni1−xPtxSi phase nucleation and growth mechanisms, Microelectronic Engineering. 244–246 (2021) 111571. https://doi.org/10.1016/j.mee.2021.111571.
[18] L. Lachal, P. Rodriguez, M. Grégoire, E. Ghegin, F. Milesi, M. Coig, J. Borrel, S. Joblot, M. Juhel, F. Nemouchi, F. Mazen, Effects of Pre-amorphization Thickness and Carbon Implantation on NiPt/Si Silicidation Process, in: 2018 22nd International Conference on Ion Implantation Technology (IIT), 2018: pp. 54–57. https://doi.org/10.1109/IIT.2018.8807963.
[19] A.S. Ozcan, D. Wall, J. Jordan-Sweet, C. Lavoie, Effects of temperature dependent pre-amorphization implantation on NiPt silicide formation and thermal stability on Si(100), Applied Physics Letters. 102 (2013) 172107. https://doi.org/10.1063/1.4801928.
[20] Sentaurus Process User Guide, Version H-2013.03, Sentaurus, 2013.
[21] R. Yang, N. Su, P. Bonfanti, J. Nie, J. Ning, T.T. Li, Advanced in situ pre-Ni silicide (Siconi) cleaning at 65nm to resolve defects in NiSix modules, Journal of Vacuum Science & Technology B. 28 (2010) 56–61. https://doi.org/10.1116/1.3271334.
[22] F. Panciera, K. Hoummada, M. Gregoire, M. Juhel, D. Mangelinck, Pt redistribution in N-MOS transistors during Ni salicide process, Microelectronic Engineering. 107 (2013) 173–177. https://doi.org/10.1016/j.mee.2013.01.029.
[23] K. Toman, The structure of Ni2Si, Acta Crystallographica. 5 (1952) 329–331. https://doi.org/10.1107/S0365110X52001003.
[24] C. Delwail, S. Joblot, F. Mazen, F. Abbate, L. Lachal, F. Milesi, M. Bertoglio, A.M. Papon, M. Gregoire, P.H. Rodriguez, D. Mangelinck, Impact of the pre amorphization by Ge implantation on Ni0.9Pt0.1 silicide, Microelectronic Engineering. 254 (2022) 111705. https://doi.org/10.1016/j.mee.2021.111705.
[25] F. Panciera, La sonde atomique tomographique : applications aux dispositifs CMOS avancés sub-45nm, PhD, Aix-Marseille University, 2012.
[26] K. Hoummada, C. Perrin-Pellegrino, D. Mangelinck, Effect of Pt addition on Ni silicide formation at low temperature: Growth, redistribution, and solubility, Journal of Applied Physics. 106 (2009) 063511. https://doi.org/10.1063/1.3204948.
[27] M. El Kousseifi, K. Hoummada, T. Epicier, D. Mangelinck, Direct observation of NiSi lateral growth at the epitaxial θ-Ni2Si/Si(1 0 0) interface, Acta Materialia. 99 (2015) 1–6. https://doi.org/10.1016/j.actamat.2015.07.062.
[28] D. Mangelinck, Chapter 9 - The Growth of Silicides and Germanides, in: Handbook of Solid State Diffusion, Volume 2, Elsevier, 2017: pp. 379–446. https://doi.org/10.1016/B978-0-12-804548-0.00009-8.
[29] R.B. Schwarz, W.L. Johnson, Formation of an Amorphous Alloy by Solid-State Reaction of the Pure Polycrystalline Metals, Physical Review Letters. 51 (1983) 415–418. https://doi.org/10.1103/PhysRevLett.51.415.
[30] B. Imbert, M. Gregoire, S. Zoll, R. Beneyton, S. Del-Medico, C. Trouiller, O. Thomas, Nitrogen impurity effects on nickel silicide formation at low temperatures – New “nitrogen co-plasma” approach, Microelectronic Engineering. 85 (2008) 2005–2008. https://doi.org/10.1016/j.mee.2008.04.021.
[31] E. Ma, C.W. Nieh, M.-A. Nicdlet, W.L. Johnson, Solid-state amorphization reaction by temperature-dependent ion mixing, Journal of Materials Research. 4 (1989) 1299–1302. https://doi.org/10.1557/JMR.1989.1299.
[32] D. Ma, D.Z. Chi, M.E. Loomans, W.D. Wang, A.S.W. Wong, S.J. Chua, Kinetics of NiSi-to-NiSi2 transformation and morphological evolution in nickel silicide thin films on Si(001), Acta Materialia. 54 (2006) 4905–4911. https://doi.org/10.1016/j.actamat.2006.06.042.

[33] J.W. Christian, The Theory of Transformations in Metals and Alloys, Newnes, 2002.
[34] D.A. Porter, K.E. Easterling, Phase Transformations in Metals and Alloys, Third Edition (Revised Reprint), CRC Press, 1992.
[35] M.S. Westwell, M.S. Searle, D.J. Wales, D.H. Williams, Empirical Correlations between Thermodynamic Properties and Intermolecular Forces, J. Am. Chem. Soc. 117 (1995) 5013–5015. https://doi.org/10.1021/ja00123a001.
[36] T.B. Massalski, H. Okamoto, ASM International, Binary alloy phase diagrams, ASM International, Materials Park, Ohio, 1990.
[37] P. Villars, H. Okamoto, A. Prince, Handbook of Ternary Alloy Phase Diagrams, ASM International, 1995.
[38] F.M. d'Heurle, Nucleation of a new phase from the interaction of two adjacent phases: Some silicides, Journal of Materials Research. 3 (1988) 167–195. https://doi.org/10.1557/JMR.1988.0167.
[39] L. Ehouarne, Métallisation des mémoires Flash à base de NiSi et d'éléments d'alliages, PhD, University Aix-Marseille III, 2008. https://theses.hal.science/tel-00408377.
[40] B.E. Deal, A.S. Grove, General Relationship for the Thermal Oxidation of Silicon, Journal of Applied Physics. 36 (1965) 3770. https://doi.org/10.1063/1.1713945.
[41] F. Nemouchi, D. Mangelinck, C. Bergman, P. Gas, U. Smith, Differential scanning calorimetry analysis of the linear parabolic growth of nanometric Ni silicide thin films on a Si substrate, Applied Physics Letters. 86 (2005) 041903. https://doi.org/10.1063/1.1852727.
[42] K. Tu, J.W. Mayer, L.C. Feldman, Electronic Thin Film Science: For Electrical Engineers and Materials Scientists, Macmillan, 1992.
[43] K.-N. Tu, A.M. Gusak, Kinetics in Nanoscale Materials, John Wiley & Sons, 2014.
[44] L.J. Chen, Solid state amorphization in metal/Si systems, Materials Science and Engineering: R: Reports. 29 (2000) 115–152. https://doi.org/10.1016/S0927-796X(00)00023-1.
[45] F. Faupel, W. Frank, M.-P. Macht, H. Mehrer, V. Naundorf, K. Rätzke, H.R. Schober, S.K. Sharma, H. Teichler, Diffusion in metallic glasses and supercooled melts, Rev. Mod. Phys. 75 (2003) 237–280. https://doi.org/10.1103/RevModPhys.75.237.
[46] T. Barge, P. Gas, F.M. d'Heurle, Analysis of the diffusion controlled growth of cobalt silicides in bulk and thin film couples, Journal of Materials Research. 10 (1995) 1134–1145. https://doi.org/10.1557/JMR.1995.1134.
[47] P. Gas, F.M. D'Heurle, Diffusion in Silicide, in: Diffusion in Semiconductors and Non-Metallic Solids, Ed. D.L. Beke, Springer Verlag, Berlin, 1998.
[48] M. El Kousseifi, K. Hoummada, T. Epicier, D. Mangelinck, Ni silicides formation: use of Ge and Pt to study the diffusing species, lateral growth and relaxation mechanisms., in: 2015 IEEE International Interconnect Technology Conference and 2015 IEEE Materials for Advanced Metallization Conference (IITC/MAM) Pages: 257-259 Published: 2015, Ieee, New York, 2015: pp. 257–259.
[49] F. Nemouchi, D. Mangelinck, J.L. Lábár, M. Putero, C. Bergman, P. Gas, A comparative study of nickel silicides and nickel germanides: Phase formation and kinetics, Microelectronic Engineering. 83 (2006) 2101–2106. https://doi.org/10.1016/j.mee.2006.09.014.
[50] I. Park, J.B. Seol, G. Yoon, J.-S. Lee, Three-dimensional imaging of carbon clusters in thermally stable nickel silicides by carbon pre-implantation, Applied Surface Science. 539 (2021) 148152. https://doi.org/10.1016/j.apsusc.2020.148152.

Appendix A: Characteristic of the amorphous layer according to the PAI parameter.

The PAI parameters were determined by TCAD simulation with the KMC (Kinetic Monte Carlo) model using the Synopsys Sentaurus process simulator. For each sample, the a-Si thickness, and the concentration at the Rp are calculated by simulation. Table A-1 gives an overview of the PAI parameters, and the characteristics of the amorphous layer induced.

Table A-1 : Overview of the PAI parameters and characteristics of the induced amorphous layers

	PAI parameters			Characteristic of the amorphous layer		
Sample	Implanted specie	Fluence (at/cm²)	Energy (keV)	**a-Si thickness (nm)**	**Rp (nm)**	**Concentration at Rp (at/cm³)**
Q1	Ge	$1x10^{14}$	20	**25**	**16**	**$4.5x10^{19}$**
Q2	Ge	$9x10^{14}$	13	**25**	**11**	**$6x10^{20}$**
Q3	Ge	$9x10^{14}$	13	**25**	**11**	**$6x10^{20}$**
	C	$4X10^{15}$	3		**8,5**	**$2x10^{21}$**

Appendix B: XRR model and fits used to determine the silicide thickness.

For this work, the silicide thickness accuracy needs to be extremely high (~0.1 nm). Such accuracy of the layer thickness can be reached by XRR analyses thanks to the layered structure, the silicide morphology, and the knowledge of the reference silicide composition (i.e., Pt gradient determined by Panciera et. al by APT [11] [22]). Indeed, the XRR measurement is realized after the metal etching, thus, the layered structure is only composed of the silicon substrate, the silicide, and the native oxide. Moreover, as the silicide is amorphous, it is less rough than a crystalline silicide layer. By considering these layers and the Pt gradient in the silicide, a very good fit can be obtained and the accuracy in the layer thickness is high (0.1 nm).

For example, fig. 2 shows the XRR model (red curve) and the experimental result (blue curve) obtained for the reference sample. Fig. 2, b shows that a shift of 0.1 nm of the silicide thickness induces a horizontal shift of the model. The periods of the oscillation are no longer superimposed. However, fig. 2, c, d e show that if the silicide density, roughness or even the thickness of the native oxide are slightly modified, the oscillations are shifted but the angles corresponding at the period of the oscillation remain the same. In conclusion, for our sample, the XRR measurement is efficient to precisely determine the silicide thickness but is less efficient to precisely determine the silicide density or roughness due to the multiplication of the modelized layers and to the induced parameters.

a)

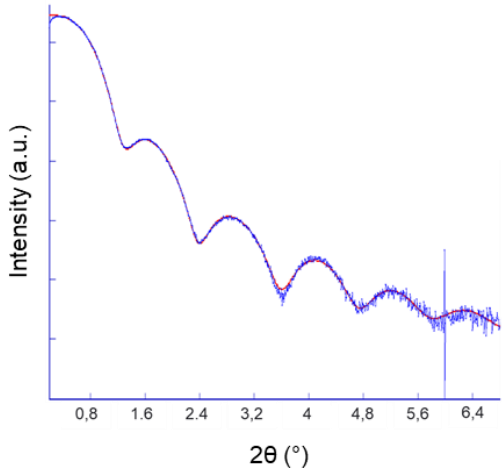

Layer	Thickness (nm)	Density (g/cm³)	Roughness (nm)
SiO_2	1.5	2.2	0.3
$Ni_{0.57}Si_{0.28}Pt_{0.15}$	1.7	10.1	0.2
$Ni_{0.57}Si_{0.38}Pt_{0.05}$	1.5	8.1	0.3
$Ni_{0.6}Si_{0.4}$	4.4	6.7	0.9
Si	substrate	2.330	0.4

b)

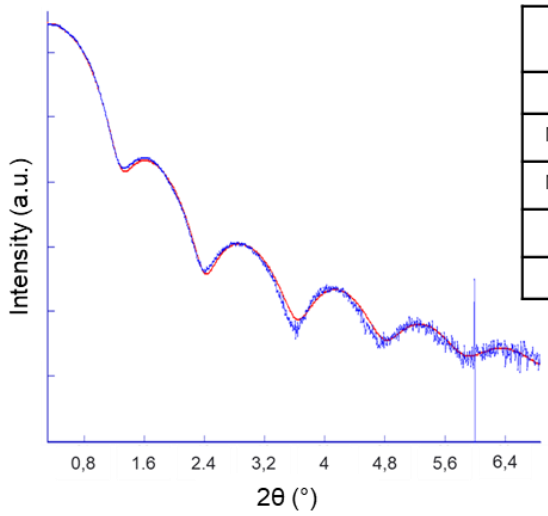

Layer	Thickness (nm)	Density (g/cm^3)	Roughness (nm)
SiO_2	1.5	2.2	0.3
$Ni_{0.57}Si_{0.28}Pt_{0.15}$	1.7/1.6	10.1	0.2
$Ni_{0.57}Si_{0.38}Pt_{0.05}$	1.5	8.1	0.3
$Ni_{0.6}Si_{0.4}$	4.4	6.7	0.9
Si	substrate	2.330	0.4

c)

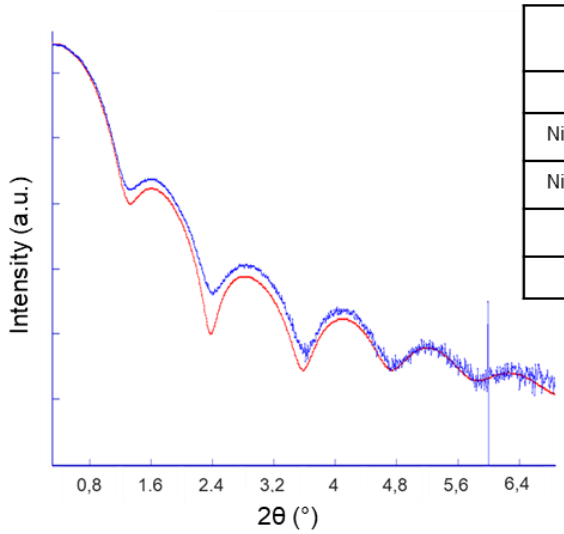

Layer	Thickness (nm)	Density (g/cm^3)	Roughness (nm)
SiO_2	1.5	2.2	0.3
$Ni_{0.57}Si_{0.28}Pt_{0.15}$	1.7	10.1/9.1	0.2
$Ni_{0.57}Si_{0.38}Pt_{0.05}$	1.5	8.1	0.3
$Ni_{0.6}Si_{0.4}$	4.4	6.7	0.9
Si	substrate	2.330	0.4

d)

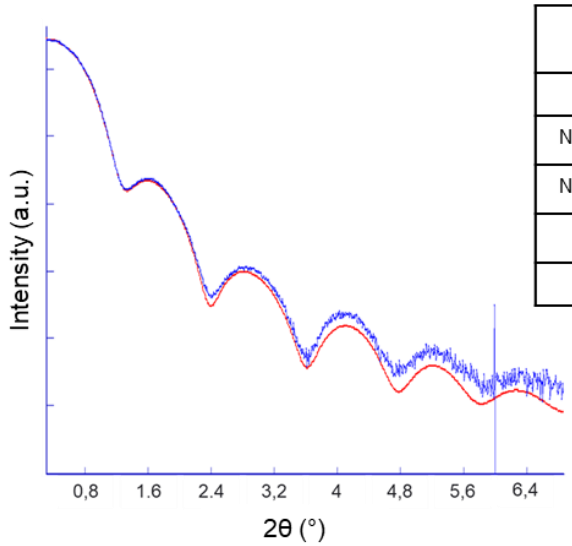

Layer	Thickness (nm)	Density (g/cm^3)	Roughness (nm)
SiO_2	1.5	2.2	0.3
$Ni_{0.57}Si_{0.28}Pt_{0.15}$	1.7	10.1	0.2/0.3
$Ni_{0.57}Si_{0.38}Pt_{0.05}$	1.5	8.1	0.3
$Ni_{0.6}Si_{0.4}$	4.4	6.7	0.9
Si	substrate	2.330	0.4

e)

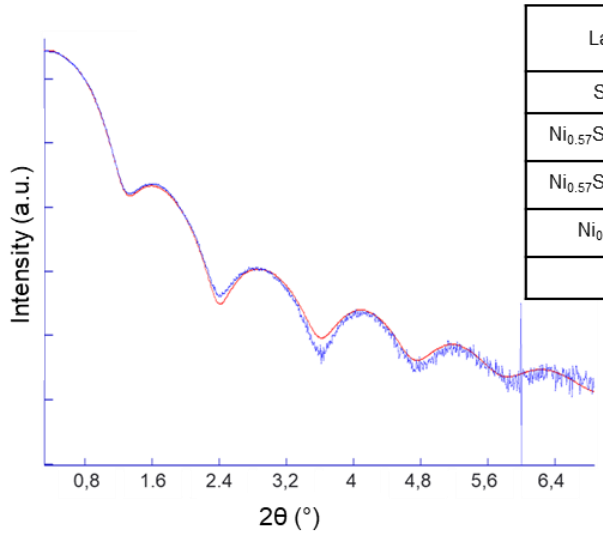

Layer	Thickness (nm)	Density (g/cm³)	Roughness (nm)
SiO_2	1.5/1.6	2.2	0.3
$Ni_{0.57}Si_{0.28}Pt_{0.15}$	1.7	10.1	0.2
$Ni_{0.57}Si_{0.38}Pt_{0.05}$	1.5	8.1	0.3
$Ni_{0.6}Si_{0.4}$	4.4	6.7	0.9
Si	substrate	2.330	0.4

Fig. 1. X-ray reflectivity curves (XRR) for the reference sample (blue curve) and the model used (red curve) to determine the silicide thickness. a) represents the result of the simulation for the reference sample, while the influence of a slight variation of the silicide b) thickness (0.1nm), c) density, d) roughness, and also e) the thickness of the native oxide; are represented to illustrate their impact on the shape of the XRR curve.

Appendix C: Transformation curve for the Temperature Time Transformation diagram

The kinetics of the amorphous-to-crystalline silicide transformation was analyzed in terms of the classical theories of nucleation and growth [32–34]. Since large grains (larger than the APT sample size, i.e., larger than 20nm) were found for the θ-Ni_2Si phase [11], the amorphous-to-crystalline silicide transformation was considered as a two-dimensional phase transformation process. In this case, the volume fraction (f) of transformed θ-Ni_2Si can be expressed by [32,33]:

$$f = 1 - exp(-c_1 \delta I U^2 t^3) \qquad \textit{Eq. A.1}$$

where δ is the thickness of the amorphous silicide film, $c_1 = \pi/3$, I the nucleation rate, U the growth rate, and t the time. According to classical nucleation theory [32–34], the steady-state nucleation rate for θ-Ni_2Si nucleation can be written as:

$$I = I_0 exp\left(-\frac{\Delta G^*(T)}{kT}\right) exp\left(-\frac{Q_n}{kT}\right) = \frac{\omega n^{\frac{2}{3}}}{\delta} exp\left(-\frac{\Delta G^*(T)}{kT}\right) exp\left(-\frac{Q_n}{kT}\right) \qquad \textit{Eq. A.2}$$

Where I_0 is the number of atoms in contact with nucleation sites per unit of volume, n is the number of potential nucleation sites per unit volume, k the Boltzmann's constant, T the temperature, and Q_n is the activation energy for atomic migration required during nucleation. ω is a characteristic frequency

that should be in the order of the Debye frequency. The nucleation barrier, $\Delta G^*(T)$, is given by the expression $\Delta G^*(T) = c_2 \Delta\sigma^3 / \Delta G_V^2$, where c_2 is a geometrical term [38]. $\Delta\sigma$ is the effective interfacial energy change accompanying nucleation [38]. ΔG_V is the Gibbs free energy change per unit volume of θ-Ni_2Si formed and can be approximated by [34]:

$$\Delta G_V = \frac{1}{\Omega}\frac{\mathrm{L}}{T_m}(T - T_m) \qquad \textit{Eq. A.3}$$

where T_m is the melting point of the θ-Ni_2Si phase, L is the latent heat of fusion, and Ω is the atomic volume.

The average growth rate (U) for θ-Ni_2Si growing laterally into the amorphous silicide can be approximated by [32,33]

$$U = \frac{a_0 \omega \Delta g_a}{kT} exp\left(-\frac{Q_g}{kT}\right) \qquad \textit{Eq. A.4}$$

where a_0 is the distance across the growing interface, Q_g is the activation energy for atomic migration required during incoherent growth. Δg_a is the driving force for transformation per reacting atom and can be approximated [32,33] as $\Delta g_a = \Delta G_V \Omega$.

Combining Eq. A1 - A4, we define the following function:

$$f = 1 - exp\left(-c_3\left(\frac{\Delta g_a}{kT}\right)^2 exp\left(-\frac{\Delta G^*(T) + Q_n + 2Q_g}{kT}\right)t^3\right) \qquad \textit{Eq. A.5}$$

In first approximation, Q_n can be considered equal to Q_g since they both correspond to an energy for atoms to cross the amorphous/crystalline interface. Within these assumptions, Eq. A.5 becomes:

$$f = 1 - exp\left(-c_4\left(\frac{\Delta G_V}{kT}\right)^2 exp\left(-\frac{c_2 \Delta\sigma^3 / \Delta G_V^2 + 3Q_g}{kT}\right)t^3\right) = 1 - exp(-K(T)t^3) \qquad \textit{Eq. A.6}$$

Where the term $K(T)$ that depends only on temperature is given by:

$$K(T) = c_4\left(\frac{\Delta G_V}{kT}\right)^2 exp\left(-\frac{c_2 \Delta\sigma^3 / \Delta G_V^2 + 3Q_g}{kT}\right) \qquad \textit{Eq. A.7}$$

Where the c_4 constant is expressed as:

$$c_4 = \frac{\pi}{3}\,\Omega^2 n^{\frac{2}{3}}\, a_0^2\, \omega^3 \qquad \textit{Eq. A.8}$$

By setting f to a given value (for example, 1% that is the usual resolution limit for phase detection), the time at a given temperature is expressed as:

$$t = (-\ln(1-f)/K(T))^{1/3} \qquad \textit{Eq. A.9}$$

Appendix D: Nonlinear reactive diffusion

Fig. B.1 [43] schematically describes diffusion with or without a driving force gradient. This figure represents the potential energy in a crystal lattice: this energy is periodic with the periodicity of the lattice, the minima corresponding to the atomic positions of equilibrium and the maxima to the neck positions that the atoms must cross to diffuse (Fig. B.1.a). The difference between these minima and maxima corresponds to the diffusion activation energy (ΔG_m). Without a driving force gradient (= energy gradient), all the minima are at the same energy but when a driving force gradient is applied, the energy of the minima depends on the position (Fig. B.1.b).

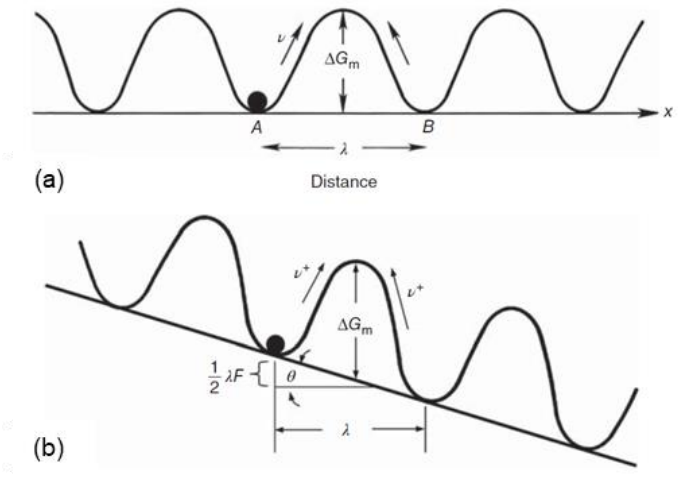

Fig. B.1. Diffusion (a) without or (b) with driving force gradient (reproduction from [43])

In a material, the atoms vibrate with a frequency, ν_0, of the order of the Debye frequency around their equilibrium position. The jump probability between an equilibrium position and the next position is proportional to the neck energy according to the law of thermally activated phenomena:

$$p = \exp\left[\frac{-\Delta G_m}{kT}\right] \qquad \textit{Eq. B.1}$$

With, k the Boltzmann constant, and T the temperature of the system.

The jump frequency Γ is then the product of this probability by the attack (vibration) frequency:

$$\Gamma = \nu_0\, p = \nu_0 \exp\left[\frac{-\Delta G_m}{kT}\right] \qquad \textit{Eq. B.2}$$

The net frequency between two adjacent atomic positions, Γ_n, is expressed by:

$$\Gamma_n = \Gamma^+ - \Gamma^- \qquad \textit{Eq. B.3}$$

where Γ^+ et Γ^- represent the jump frequencies to positive and negative x-axis respectively.

In the absence of gradient, these two frequencies are equal, the net frequency is zero and there is no net transport.

On the other hand, if a driving force gradient is present, the net frequency is expressed by:

$$\Gamma_n = \Gamma^+ - \Gamma^- = \nu_0 \exp\left[\frac{-\Delta G_m + \lambda F/2}{kT}\right] - \nu_0 \exp\left[\frac{-\Delta G_m - \lambda F/2}{kT}\right] = 2\Gamma \sinh\left[\frac{\lambda F}{2kT}\right] \qquad \textit{Eq. B.4}$$

where, Γ_n is the net transport frequency, Γ the probability of finding a defect multiplied by the jumping atoms frequency, λ the jump distance, F the driving force. According to the limited development and the values of the hyperbolic sine function the transport frequency can be simplified according to the following relations.

$$\sinh[x] \approx x + \frac{x^3}{3!} \qquad \textit{Eq. B.5}$$

When the driving force is small compared to λ/kT (x very small), the term in x^3 becomes negligible and the net frequency is proportional to the driving force.

$$if\ \frac{\lambda F}{2kT} << 1 \quad \Rightarrow \Gamma_n = \Gamma \frac{\lambda F}{kT} \qquad \textit{Eq. B.6}$$

In this case (linear approximation), the net frequency therefore varies linearly with the driving force, and we find the Nernst-Einstein equation considering that the diffusion coefficient is $D = \lambda^2 \Gamma$.

$$J = Cv = C\lambda\Gamma_n = C\Gamma\frac{\lambda^2 F}{kT} = \frac{CD}{kt}F \qquad \textit{Eq. B.7}$$

where, J is the diffusion flux, C the concentration of atoms, v the migration velocity. In the usual case where the driving force is of chemical origin, we have:

$$F = -\frac{d\mu}{dz} \approx -\frac{\Delta\mu}{L} \qquad \textit{Eq. B.8}$$

where $d\mu/dz$ is the chemical potential gradient.

$$J = -\frac{CD}{kT}\frac{d\mu}{dz} \qquad \textit{Eq. B.9}$$

In addition, the growth rate (dL/dt) depends on the molecular volume Ω and the diffusion flux according to the following equation:

$$\frac{dL}{dt} = \Omega J = \frac{1}{C}J \qquad \textit{Eq. B.10}$$

Therefore, in the case of the linear approximation, the growth rate of the thin film can be expressed as:

$$\frac{dL}{dt} = \frac{D}{k_B T}\frac{d\mu}{dz} \approx \frac{D}{k_B T}\frac{\Delta\mu}{L} = \frac{K_D}{L} \qquad \textit{Eq. B.11}$$

Eq. B.11 corresponds to the classical law of growth controlled by diffusion.

In the general case, the flux and growth rate can be expressed as:

$$J = C\lambda\Gamma_n = 2\frac{CD}{\lambda}\sinh\left[\frac{\lambda F}{2kT}\right] = 2\frac{CD}{\lambda}\sinh\left[\frac{\lambda}{2kT}\frac{\Delta\mu}{L}\right] \qquad \textit{Eq. B.12}$$

$$\frac{dL}{dt} = 2\frac{D}{\lambda}\sinh\left[\frac{\lambda F}{2kT}\right] \qquad \textit{Eq. B.13}$$

$$\frac{dL}{dt} = 2\frac{D}{\lambda}\sinh\left[\frac{\lambda}{2kT}\frac{\Delta\mu}{L}\right] \; \frac{dL}{dt} = a_{sh}sinh\left[\frac{b_{sh}}{L}\right] \qquad \textit{Eq. B.14}$$

where, a_{sh} et b_{sh} are the nonlinear coefficients.

Eq. B.14 can be called nonlinear reactive diffusion law. While the equations for nonlinear diffusion (Eq. B.12 to B.16) are well established [43], the application to phase growth by reactive diffusion has not been previously established to our knowledge.

If the driving force gradient is large, the second term of the limited expansion of the hyperbolic sine can no longer be neglected. Therefore, the net frequency (Γ_n) is related to the driving force (F) by the following relation:

$$\Gamma_n = 2\Gamma\left(\frac{\lambda F}{2kT} + \frac{1}{6}\left(\frac{\lambda F}{2kT}\right)^3\right) \qquad \textit{Eq. B.15}$$

Therefore, the diffusion flux (J) can be expressed as:

$$J = Cv = C\Gamma\lambda^2\left(\frac{F}{kT} + \frac{\lambda^2}{24}\left(\frac{F}{kT}\right)^3\right) \qquad \textit{Eq. B.16}$$

If the driving force is equal to the chemical potential gradient, the diffusion flux (J) is:

$$J = Cv = CD\left(\frac{\Delta\mu}{kT}\frac{1}{L} + \frac{\lambda^2}{24}\left(\frac{\Delta\mu}{kT}\right)^3\frac{1}{L^3}\right) \qquad \textit{Eq. B.17}$$

From equation 4. B.10, the growth rate (dL/dt) s then expressed by:

$$\frac{dL}{dt} = D\left(\frac{\Delta\mu}{kT}\frac{1}{L} + \frac{\lambda^2}{24}\left(\frac{\Delta\mu}{kT}\right)^3\frac{1}{L^3}\right) = \frac{K_D}{L} + \frac{b_{nl}}{L^3} \qquad \textit{Eq. B.18}$$

where, a_{nl} et b_{nl} are the kinetics coefficients of the nonlinear coefficient.

From Eq. B.17, two limit cases can be defined depending on whether the chemical potential gradient is high or relatively low. As the chemical potentials are fixed by the equilibria at the interfaces, $\Delta\mu$ is constant and the chemical potential gradient only depends on the inverse of the phase thickness.

If the thickness (L) is large (low gradient), the term inversely proportional to the cube of the thickness (Eq. B.17) becomes negligible and the growth rate can be expressed according to the following relationship:

$$\frac{dL}{dt} = D\left(\frac{\Delta\mu}{kT}\frac{1}{L} + \frac{\lambda^2}{24}\left(\frac{\Delta\mu}{kT}\right)^3\frac{1}{L^3}\right) = D\frac{\Delta\mu}{kT}\frac{1}{L} = \frac{K_D}{L} \qquad \textit{Eq. B.19}$$

We find again the classic equation of formation controlled by “linear” diffusion.

The integration of Eq. B.18 classically leads to a thickness proportional to the square root of time, which corresponds to a parabolic growth:

$$LdL = K_D dt \Rightarrow L^2 - L_0^2 = \frac{K_D}{2}t = D\,\frac{\Delta\mu}{2kT}t = \frac{Da_{nl}}{2}t \Rightarrow L \propto t^{1/2} \qquad \textit{Eq. B.20}$$

The nonlinear reactive diffusion therefore leads us to the same conclusion as the linear diffusion when the thickness of silicide is important (parabolic growth).

If the thickness (L) is small (strong gradient), it is the term inversely proportional to the thickness which becomes negligible in the equation Eq. B.17:

$$\frac{dL}{dt} = D\left(\frac{\Delta\mu}{kT}\frac{1}{L} + \frac{\lambda^2}{24}\left(\frac{\Delta\mu}{kT}\right)^3\frac{1}{L^3}\right) = D\frac{\lambda^2}{24}\left(\frac{\Delta\mu}{kT}\right)^3\frac{1}{L^3} = \frac{b_{nl}}{L^3} \qquad \textit{Eq. B.21}$$

Integrating the equation gives a thickness proportional to time at the fourth root :

$$L^3 dL = b_{nl} dt \Rightarrow L^4 - L_0^4 = \frac{b_{nl}}{4}t \Rightarrow L \propto t^{1/4} \qquad \textit{Eq. B.22}$$

Eq. B.22 is only a rough approximation and should be used carefully since Eq. B.14 is the general law. However, Eq. B.22 provides an easy way to estimate if the nonlinear reactive diffusion law should be used as detailed in the discussion.